American Mineralogist, Volume 109, pages 1443–1460, 2024

Chemical and boron isotopic composition of tourmaline from the Yixingzhai gold deposit, North China Craton: Proxies for ore fluids evolution and mineral exploration

Shao-Rui Zhao[1,2,†], Hao Hu[1], Xiao-Ye Jin[1,2,*], Xiao-Dong Deng[1,‡], Paul T. Robinson[1,2], Wen-Sheng Gao[2], and Li-Zhong Zhang[2,3]

[1]State Key Laboratory of Geological Processes and Mineral Resources, China University of Geosciences, Wuhan 430074, China
[2]School of Earth Resources, China University of Geosciences, Wuhan 430074, China
[3]Mineral Exploration Institute, Zijin Mining Group Co., Ltd., Xiamen 361006, China

Abstract

Tourmaline is common in magmatic-hydrothermal deposits, and its composition and boron isotope geochemistry have been widely used to fingerprint the source and evolution of hydrothermal fluids and associated metals. However, whether these chemical or boron isotopic compositions or their combinations can be used as vectors for mineral exploration remains to be explored. In this study, we documented the major and trace element compositions and boron isotopic values of tourmaline along a vertical extension (i.e., 510, 830, 1230 m above sea level, a.s.l.) of the newly discovered porphyry Au mineralization in the Hewan feldspar quartz porphyry, Yixingzhai deposit, to shed light on the evolution of the ore-forming fluid, the mechanisms of Au deposition, and potential indicators for Au exploration. Field observations showed that tourmaline in the Hewan porphyry occurred mainly as orbicules or veins and intergrew with Au-bearing pyrite, hydrothermal quartz, and some clay minerals, indicating a magmatic-hydrothermal origin. Tourmaline sampled from 510 m a.s.l. showed $\delta^{11}B$ values (–11.5 to –9.3‰) consistent with those of the average continental crust and tourmaline in magmatic systems, which suggests that the ore-forming fluid was most likely exsolved from the host Hewan porphyry. The $\delta^{11}B$ values became heavier upward, reaching –9.9 to –1.5‰ at 830 m and –8.0 to +6.8‰ at 1230 m a.s.l. This boron isotopic variation, integrated with increasing Fe, Mg, Na, Ca, Li, Co, and Sr but decreasing Al, U, Th, REE, Zn, and Pb contents of the tourmaline samples from deep to shallow levels, implies that the initial magmatic fluids were gradually mixed with circulating meteoric water that contained materials leached from peripheral Archean metamorphic rocks and Mesoproterozoic marine sedimentary rocks. Considering the spatial distribution of the Au grade of the porphyry, we propose that a suitable mixing proportion of magmatic and meteoric fluids caused Au deposition and accumulation. We note that tourmaline samples collected from the economic Au zones had much lower and more concentrated $\delta^{11}B$ (–11.5 to –3.0‰), Co/(Pb+Zn) (<0.01), and Sr/(Pb+Zn) (0.27 to 1.07) values than those in low-grade or barren zones. Coeval plutons and breccia pipes, where tourmaline also occurs, are well developed inside and outside the Yixingzhai Au mine. We suggest that the obtained parameters can potentially be used as proxies for further Au exploration in this region. This study highlights the feasibility of using the chemical and isotopic compositions of tourmaline for mineral exploration.

Keywords: Tourmaline geochemistry, fluid evolution, mineral exploration, Yixingzhai Au deposit, North China Craton

Introduction

Tourmaline is a common mineral in various hydrothermal ore deposits, especially in granitoid-related, magmatic-hydrothermal deposits (e.g., Jiang et al. 2008; Dutrow and Henry 2011; Slack and Trumbull 2011; Sciuba et al. 2021). As tourmaline is stable over a wide range of temperatures and pressures and has extremely low rates of volume diffusion and high resistance to metasomatic alteration (Dutrow and Henry 2011), its microtextures, major and trace elements, and boron isotopes have been used to trace magmatic and hydrothermal processes in selected ore deposits (Slack and Trumbull 2011; van Hinsberg et al. 2011). Recent studies have also shown that its chemical and isotopic characteristics can provide insights into the mechanisms causing the associated mineral deposition (e.g., Harlaux et al. 2021; Zhao et al. 2021a), suggesting that tourmaline could be used as a guide in ore deposit exploration (e.g., Arif et al. 2010; Sciuba et al. 2021).

The Yixingzhai Au deposit in the north-central part of the North China Craton (NCC) has been explored and mined for nearly half a century (28 t Au @ 10–20 g/t; He 2014; Li et al. 2014). Recent exploration has recognized that the Hewan porphyry in the mining area is wholly mineralized, with a proven reserve of >50 t Au at an average grade of 2.3 g/t (Zhang 2018). The relevant mineralization features have been well documented and show many similarities to porphyry Au deposits (e.g., Zhang 2018; Zhang et al. 2020), but the evolution of ore-forming fluids

* Corresponding author E-mail: xiaoye.jin@cug.edu.cn.
† Orcid https://orcid.org/0000-0002-4186-7167
‡ Orcid https://orcid.org/0000-0002-3724-432X

0003-004X/24/0008–1443$05.00/DOI: https://doi.org/10.2138/am-2023-9094

and mechanisms for Au deposition remains unclear. Whether the numerous coeval plutons and cryptoexplosive breccia pipes in the mine area host similar gold mineralization remains unknown.

Tourmaline is widespread in the mineralized Hewan porphyry and other plutons/pipes in the Yixingzhai mine. In the Hewan porphyry, tourmaline is spatially related to Au-bearing pyrite, hydrothermal quartz, and sericite. These observations make tourmaline an ideal candidate to fingerprint hydrothermal fluid evolution, understand Au deposition, and potentially assist in regional Au exploration.

In this paper, we present a detailed textural, chemical, and boron isotope study of tourmaline in the Hewan porphyry to provide new insights into Au mineralization. The petrographic and textural features of tourmaline are presented to confirm its hydrothermal origin. The in situ major and trace element concentrations and boron signatures are used to trace the evolution of ore-forming fluids and investigate various mechanisms of Au deposition. Finally, the feasibility of using the chemical and boron isotopic compositions of tourmaline as guides for further Au exploration is discussed.

Geological background

The Yixingzhai Au deposit is located in the north-central domain of the Trans-North China Orogen (TNCO) of the NCC, which was formed by the collision and amalgamation of the Eastern and Western Blocks in the late Paleoproterozoic (Fig. 1a) (Zhao et al. 2005; Zhai 2011). This region is dominated by Archean metamorphic rocks, mainly tonalite-trondhjemite-granodiorite gneiss, with minor amounts of amphibolite and granulite. The protoliths of these rocks are mafic to felsic volcanic rocks interlayered with clastic rocks, all of which were metamorphosed to greenschist or amphibolite facies rocks during the formation of the TNCO (Wei 2018). These metamorphic rocks are locally overlain by Mesoproterozoic dolomites and marbles (Fig. 1b) and sporadically present marine evaporites. The Precambrian rocks are intruded, from southeast to northwest, by the Sunzhuang diorite (zircon U-Pb ages of 139 ± 1 to 134 ± 1 Ma; Li et al. 2014; Zhang et al. 2015), the Nanmenshan quartz porphyry (141 ± 1 Ma; Zhang et al. 2020), and the Hewan feldspar quartz porphyry (141 ± 1 Ma; Zhang 2018). It is noted that the Mesoproterozoic carbonate rocks are locally enclosed in the Early Cretaceous intrusions and have experienced skarn alteration (Fig. 1b). Numerous dikes, including diabase, felsite, and lamprophyre, have intruded into the mining area (Fig. 1b). They are thought to have formed at two discrete ages: the Paleoproterozoic and Early Cretaceous (Zhang 2018). The structures in the Yixingzhai mine are predominantly northwest and minor north-south trending faults, along with four cryptoexplosive

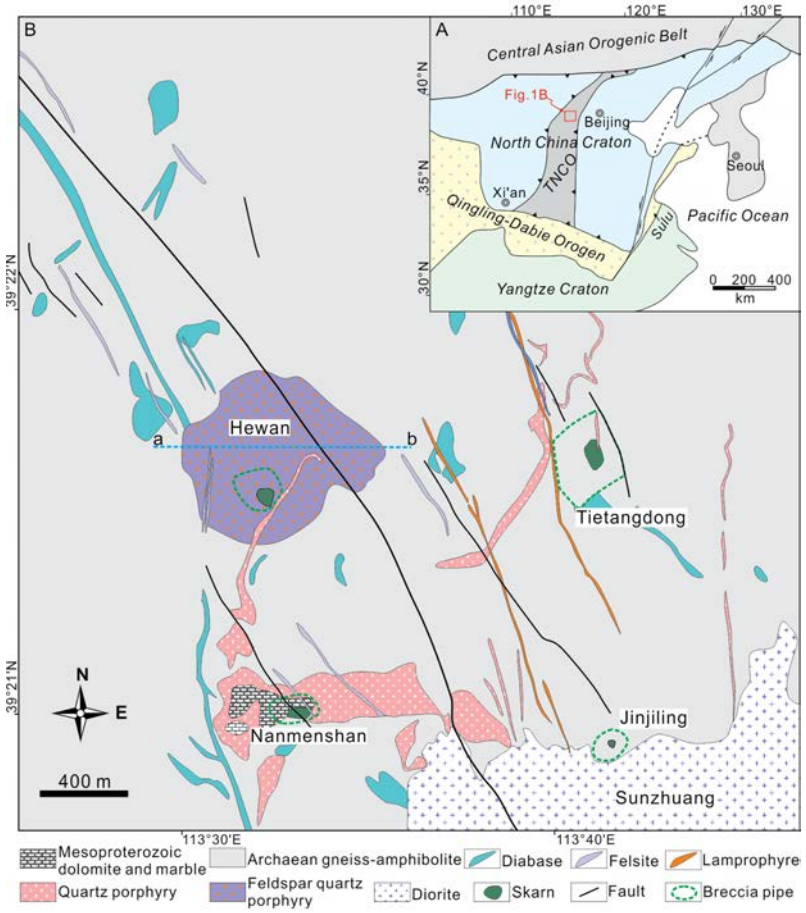

Figure 1. (**a**) The tectonic division of the NCC relative to the Yixingzhai Au deposit (modified from Zhao et al. 2005). (**b**) Geological map of the Yixingzhai Au deposit (modified from Zhang 2018). Abbreviations: TNCO = Trans-North China Orogen. (Color online.)

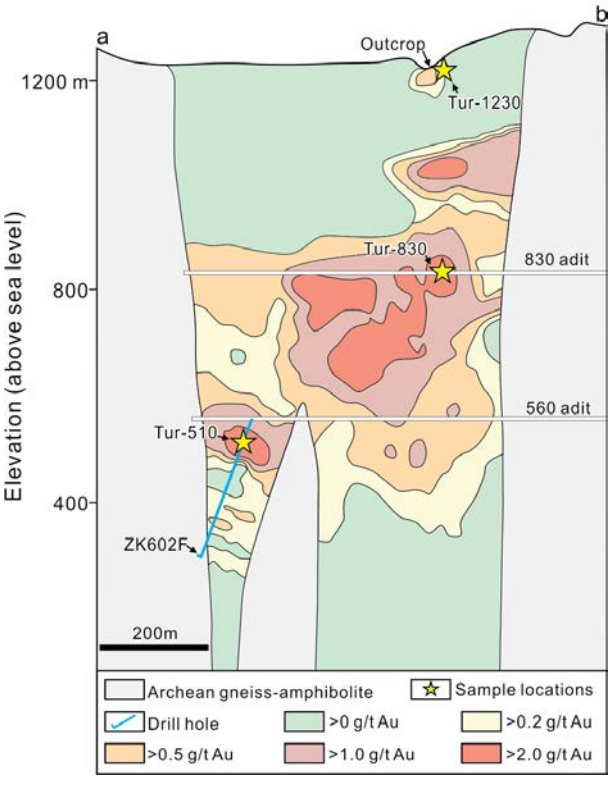

Figure 2. Geologic cross section transecting the Hewan porphyry showing the distribution of Au grade (modified from Gao 2024). Samples collected from 1230, 830, and 510 m a.s.l. are shown as Tur-1230, Tur-830, and Tur-510, respectively. (Color online.)

breccia pipes, Tietangdong, Jinjiling, Nanmenshan, and Hewan, in the mining area (Fig. 1b). Garnet and zircon U-Pb dating has constrained the timing of these four breccia pipes to approximately 140 Ma (Zhang et al. 2020).

Gold mineralization in the Hewan porphyry is characterized by interspersed pyrite disseminations and quartz-pyrite veinlets or stockworks that transect the porphyry. Relatively high grade Au ores (>1.0 g/t) are mainly present between 500 and 1100 m above sea level (a.s.l.) (Fig. 2). The ore minerals are mostly pyrite with minor amounts of chalcopyrite, sphalerite, galena, molybdenite, tetrahedrite, covellite, magnetite, and hematite. Gold occurs mainly as native Au or as electrum enclosed in pyrite (Zhang 2018). Gold mineralization is widely accompanied by potassium silicate and intermediate argillic alteration. Potassium silicate alteration is best developed below ~400 m a.s.l. and consists mainly of K-feldspar. This mineral assemblage is present in the form of dissemination, veinlets, and matrix flooding. Quartz, magnetite, and molybdenite veinlets are common in the K-silicate alteration zone. Intermediate argillic alteration is used by Vila and Sillitoe (1991) to describe the mineral assemblage of quartz-sericite-chlorite-smectite, which is accompanied by quartz veinlets, pyrite, and magnetite/hematite in the Hewan porphyry. However, the development of intermediate argillic alterations does not always indicate a high-Au grade. Potassium silicate assemblages are locally observed in and are commonly overprinted by intermediate argillic alteration. Both the K silicate and intermediate argillic alteration zones are transitional outward and upward to the propylitic and advanced argillic alteration zones, characterized mainly by chlorite-calcite-epidote and kaolinite-alunite assemblages, respectively. These two alteration zones are characterized by low-grade Au mineralization. Molybdenite Re-Os dating, coupled with garnet and zircon U-Pb dating, suggests that Au mineralization in the Hewan porphyry occurred at ca. 140 Ma (Zhang et al. 2017, 2020), coeval with the emplacement of the host porphyry and formation of breccia pipes.

Tourmaline occurrences

Field observations and drill-core logging showed that tourmaline was present from the surface to a depth of ~700 m in the Hewan porphyry (Fig. 2). The occurrences, morphologies, textures, and mineral associations of tourmaline at different levels are summarized in Table 1 and described in detail here. In the deep parts (e.g., 510 m a.s.l.; Fig. 2), tiny tourmaline crystals, chiefly along with quartz, formed small orbicular clusters that were disseminated in the mineralized porphyry (Fig. 3a). The tourmaline grains were mostly scattered in the cores of the orbicules with no observed orientation (Fig. 3b), interspersed

Table 1. Characteristics of tourmaline in the three different levels of the Hewan porphyry

	Tur-510[a]	Tur-830[b]	Tur-1230[c]
Type	Tourmaline orbicules (<0.5 cm in diameter)	Tourmaline orbicules/patches (0.5–2 cm in diameter), veins (variable in length and 5–10 cm in width)	Tourmaline orbicules (0.5–4 cm in diameter)
Occurrence	The tourmaline orbicules are disseminated in the porphyry. In the orbicules, tourmaline grains are scattered in the core and mantle with no orientation and unidirectionally accumulated along the rims.	The tourmaline orbicules/ patches are disseminated in the porphyry, whereas the tourmaline veins transect but tailout in the porphyry. Tourmaline aggregates are occasionally rimmed by leucocratic halos.	The tourmaline orbicules are disseminated in the porphyry. Quartz-tourmaline orbicules are commonly rimmed by leucocratic halos.
Morphology	Euhedral to anhedral columns, 20–200 μm in diameter, light yellow to dark blue in color	Column to lenticle in shape, 100–1000 μm in diameter, yellowish-brown to greenish-brown in color	Euhedral to subhedral, 200–1500 μm in diameters, yellowish green to dark greenish brown in color
Texture	Slightly strip-like textures in BSE images	Patchy zones in BSE images	Well-developed oscillatory zones in BSE images
Mineral association	Pyrite, sericite, quartz, chlorite, smectite, ± feldspar	Quartz, sericite, pyrite, chlorite, smectite, ± feldspar	Quartz, pyrite, sericite, ± feldspar, ± kaolinite, ± alunite

[a] Tur-510 means tourmaline samples collected from 510 m a.s.l.
[b] Tur-830 means tourmaline samples collected from 830 m a.s.l.
[c] Tur-1230 means tourmaline samples collected from 1230 m a.s.l.

with leucocratic minerals in the mantles of the orbicules, or clustered along the rims of the orbicules (Fig. 3c). In the latter case, tourmaline crystals commonly grew unidirectionally from the matrix toward the pyrite in the cores of the orbicules (Fig. 3c). Individual tourmaline crystals occurred as euhedral to anhedral columns, with grain sizes varying from 20 × 50 to 50 × 200 µm. These grains were easily recognized by their pleochroism from light yellow to dark blue (Figs. 3b–3c). Tourmaline in the orbicules coexisted spatially with pyrite, sericite, quartz, chlorite, and smectite (Figs. 3b–3e). Some quartz grains contained fluid

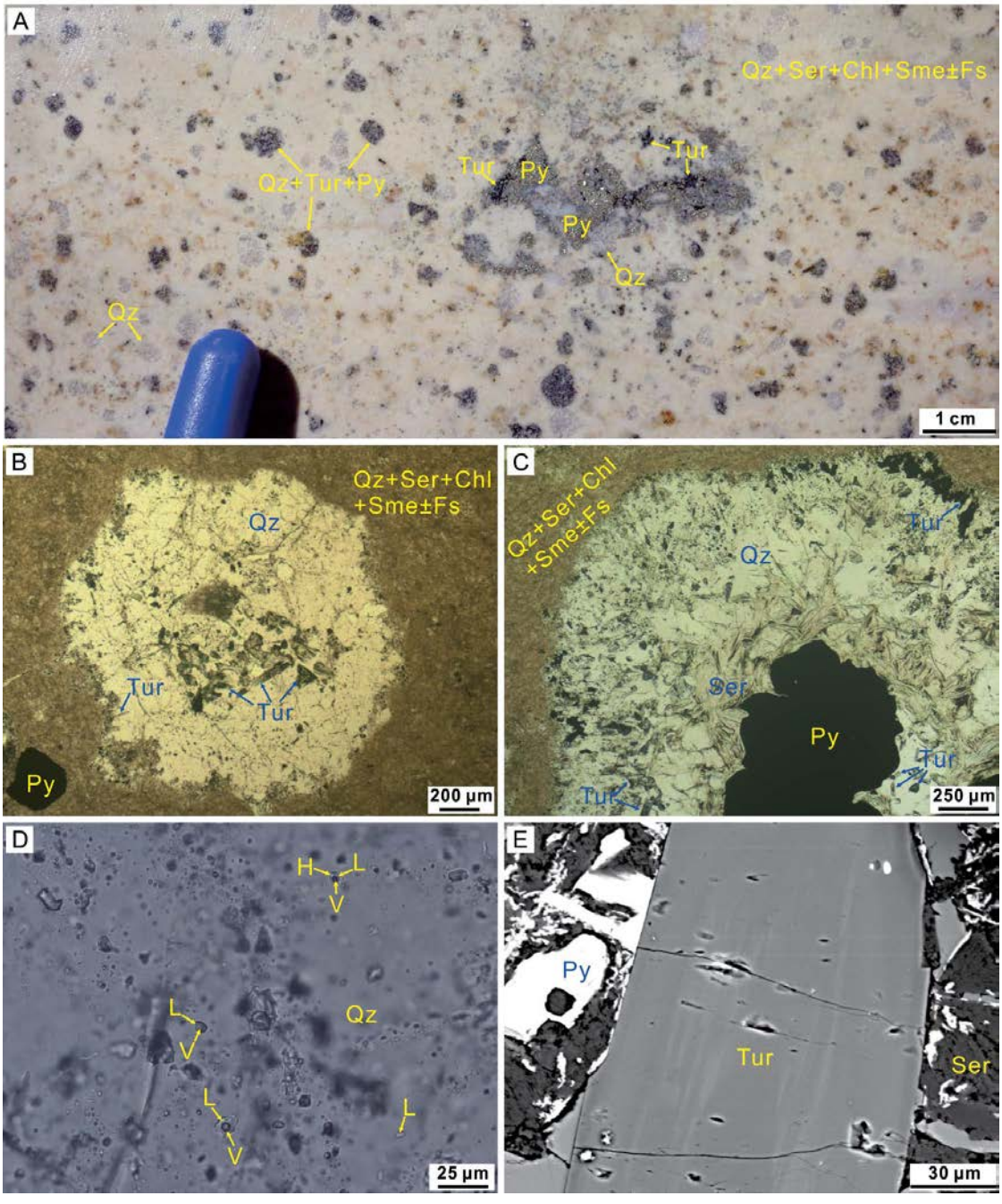

Figure 3. Photographs showing the characteristics of tourmaline present at 510 m a.s.l. of the Hewan porphyry. (**a**) Tourmaline presents in small orbicules and coexists spatially with quartz and pyrite in the porphyry. (**b**) The micrograph shows tourmaline as columns disseminated in quartz aggregates and enclosed by quartz, sericite, chlorite, smectite, and/or feldspar. (**c**) Minerals in orbicule are composed of pyrite, sericite, quartz, and tourmaline. Tourmaline scatters in the mantle or unidirectionally accumulates along rims of the orbicule. (**d**) Quartz intergrown with tourmaline contains spatially coexisted single-phase liquid, two-phase liquid-vapor, and three-phase halite-bearing fluid inclusions. (**e**) The BSE image shows tourmaline exhibiting slightly strip-like texture. Abbreviations: Qz = quartz; Tur = tourmaline; Py = pyrite; Ser = sericite; Chl = chlorite; Sme = smectite; Fs = feldspar. (Color online.)

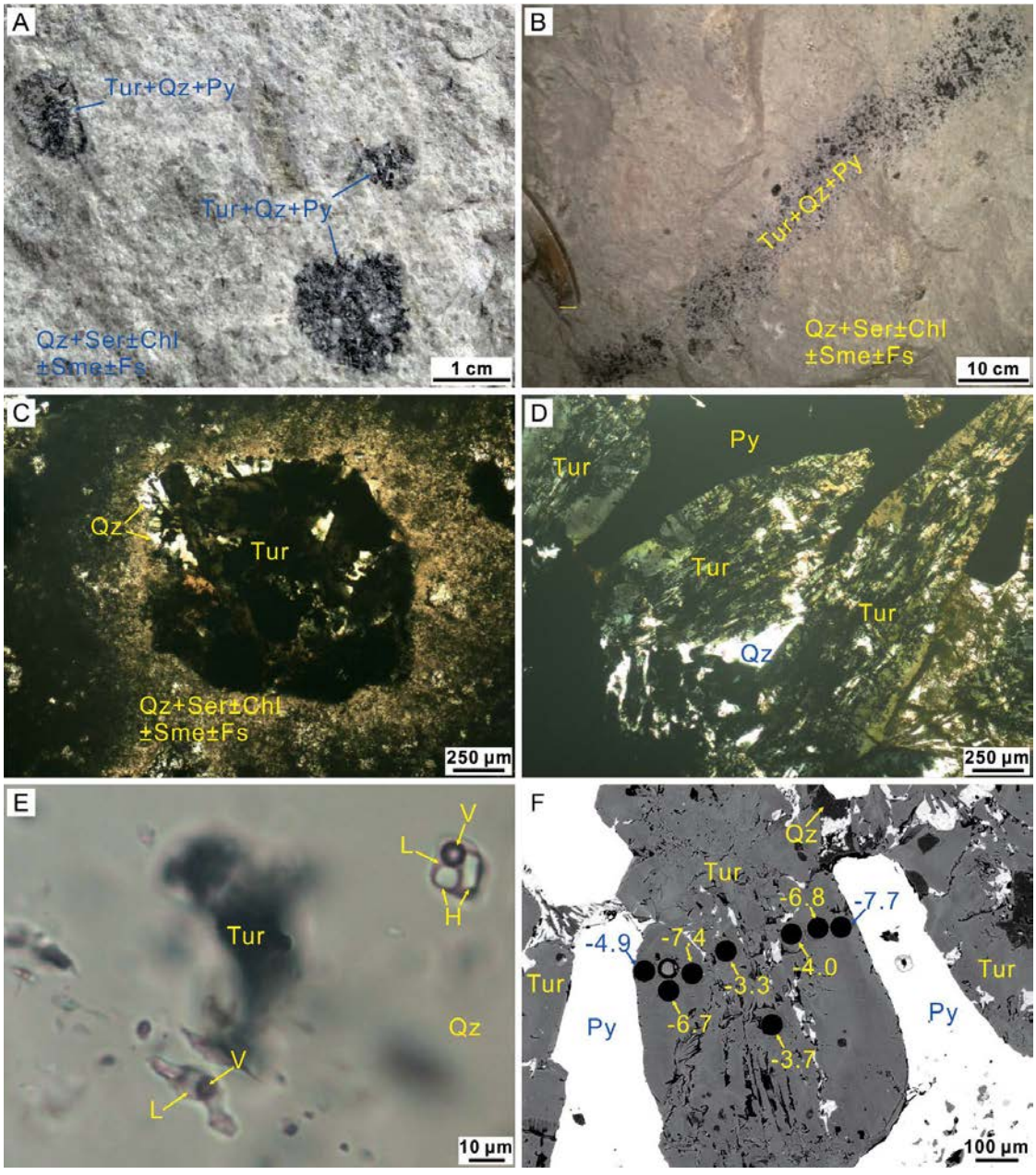

Figure 4. Photographs showing the characteristics of tourmaline from 830 m a.s.l. of the Hewan porphyry. (**a**) Tourmaline, occurring as orbicules/patches, coexists spatially with quartz and pyrite in the altered porphyry. (**b**) Tourmaline-quartz-pyrite vein transecting but tailing out in the altered porphyry. (**c**) The tourmaline-quartz orbicule is enclosed by leucocratic halo that mainly comprises quartz, sericite, chlorite, and smectite. (**d**) Greenish-brown to yellowish-brown tourmaline intergrows with pyrite and quartz. (**e**) Quartz contains tourmaline inclusion and two-phase liquid-vapor and three-phase halite-bearing fluid inclusions. (**f**) Tourmaline is closely associated with pyrite and exhibits patchy zones in the BSE image. The black dots and nearby numbers are locations of boron isotopic analyses and analytical results in per mil. Abbreviations: Qz = quartz; Tur = tourmaline; Py = pyrite; Ser = sericite; Chl = chlorite; Sme = smectite; Fs = feldspar. (Color online.)

inclusions with assemblages consisting of single-phase liquid, two-phase liquid-vapor, and three-phase liquid, vapor, and halite (Fig. 3d). In the backscattered electron (BSE) images, the tourmaline grains showed slightly strip-like textures (Fig. 3e).

Two types of tourmalines were identified in the middle parts of the Hewan porphyry (e.g., 830 m a.s.l.; Fig. 2). The first type occurred as orbicules or patches, generally 0.5 to 2 cm across, that was texturally associated with quartz and pyrite (Fig. 4a). The second type formed tourmaline-quartz-pyrite veins that transected the porphyry (Fig. 4b). These veins with variable lengths were mostly 5–10 cm wide and generally tailed out into the host porphyry where they formed structurally isolated entities.

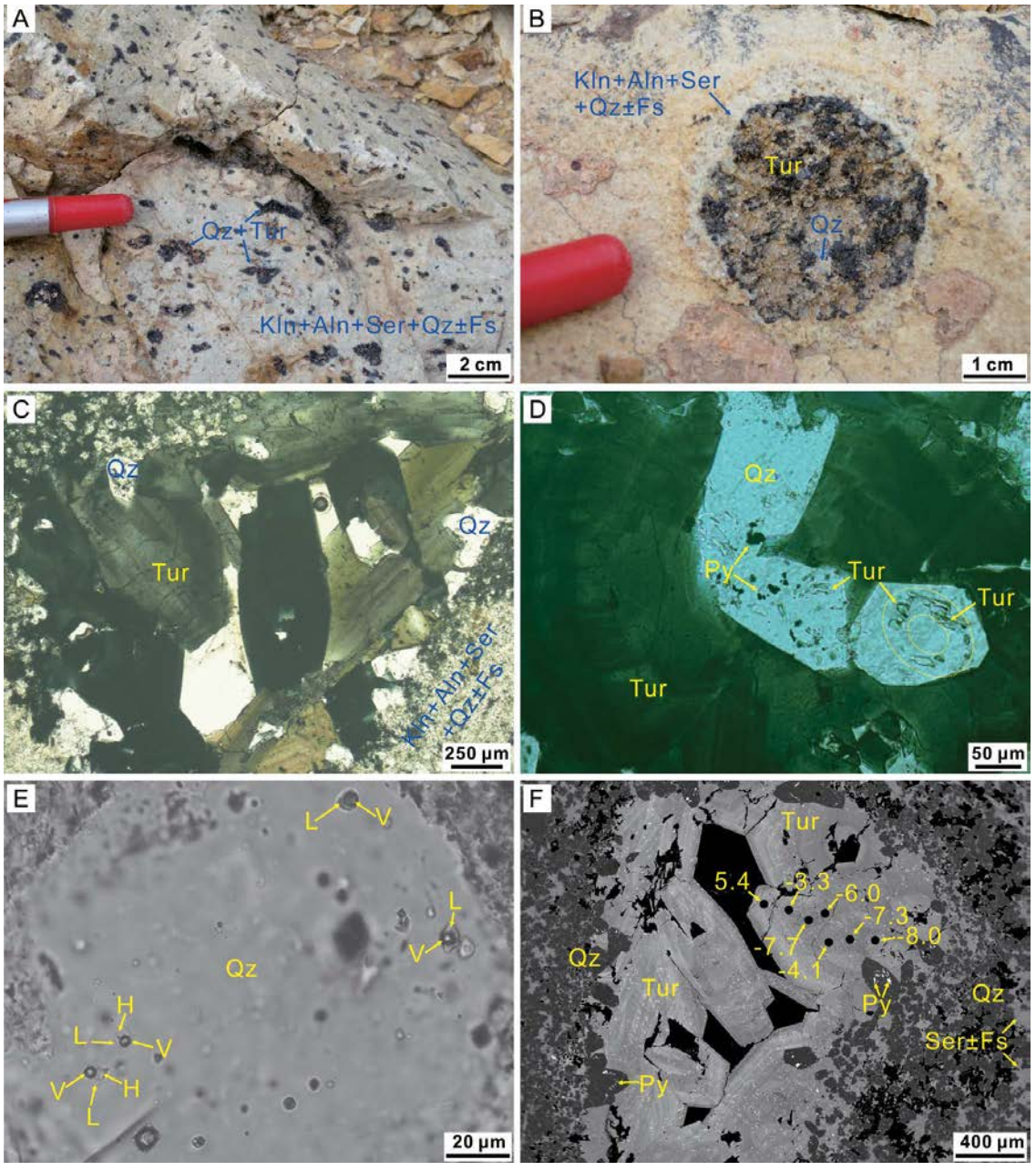

Figure 5. Photographs showing the characteristics of tourmaline from 1230 m a.s.l. of the Hewan porphyry. (**a**) Tourmaline-quartz orbicules dispersing in the altered porphyry. (**b**) Large tourmaline-quartz orbicule is rimed by leucocratic halo mineralogically dominated by kaolinite, alunite, sericite, quartz, and/or feldspar. (**c**) Euhedral to subhedral tourmaline grains are interstitial with quartz and are yellowish to dark green colors. (**d**) Greenish tourmaline intergrows with quartz. Tiny tourmaline and pyrite inclusions are encapsulated in the quartz growth zones. (**e**) Quartz in the orbicule containing two-phase liquid-vapor fluid inclusions with variable vapor/liquid ratios and halite-bearing three-phase fluid inclusions. (**f**) The BSE image shows well-developed oscillatory zones of the tourmaline. The black dots and nearby numbers are locations of boron isotopic analyses and analytical results in per mil. Abbreviations: Qz = quartz; Tur = tourmaline; Kln = kaolinite; Aln = alunite; Ser = sericite; Fs = feldspar; Py = pyrite. (Color online.)

Both types typically formed columnar to lenticular tourmaline grains with variable lengths of 100 to 1000 μm (Figs. 4a–4d). In the thin sections, some tourmaline aggregates were rimmed by leucocratic halos, which were mainly composed of fine-grained quartz and sericite, with or without chlorite, smectite, and feldspar (Fig. 4c). These tourmaline grains showed a different pleochroism, from yellowish-brown to greenish-brown (Figs. 4c–4d). Quartz intergrown with tourmaline contained abundant vapor-liquid and vapor-liquid-halite fluid inclusions (Fig. 4e). In the BSE images, tourmaline generally exhibited patchy zones

and was intimately intergrown with pyrite and quartz (Fig. 4f).

In the shallow parts of the Hewan porphyry (e.g., 1230 m a.s.l.; Fig. 2), tourmaline mainly occurred as large orbicules with diameters ranging from 0.5 to 4 cm (Figs. 5a–5b). These orbicules generally consisted of quartz and tourmaline that were surrounded by leucocratic halos with a width of 0.1–0.5 cm (Fig. 5b). The leucocratic halos were mineralogically dominated by kaolinite, alunite, sericite, quartz, and/or feldspar (Fig. 5b). Tourmaline crystals in these orbicules were euhedral to subhedral, 200–1500 µm in size, and exhibited pleochroism from yellowish green to dark greenish brown (Figs. 5c–5d). They were typically interstitial with quartz crystals (Figs. 5c–5d). In addition, tiny tourmaline and pyrite grains were observed as mineral inclusions encapsulated along the quartz growth zones (Figs. 5d–5f). The fluid inclusion assemblages in the quartz were similar to those in the samples from 510 and 830 m a.s.l. and mainly included two-phase liquid-vapor fluid inclusions with variable vapor/liquid ratios and halite-bearing three-phase fluid inclusions (Fig. 5e). In the BSE images, the tourmaline grains showed well developed oscillatory zoning and contained numerous tiny quartz inclusions (e.g., Fig. 5f).

Samples and analytical methods

Samples collected from an outcrop at ~1230 m a.s.l., an 830 m adit, and an underground drill core ZK602F at 510 m a.s.l. were investigated for textural studies (Fig. 2). The samples were prepared as standard thin sections and examined successively using an optical microscope under reflected and transmitted light and a scanning electron microscope (SEM) equipped with an energy-dispersive spectrometer (EDS). The operational conditions for SEM-EDS were set at an accelerating voltage of 20 kV and beam size of 5 µm. Subsequently, the areas of interest were selected for major (n = 102), trace (n = 53), and boron isotopic (n = 105) analyses.

The major element composition of tourmaline was analyzed using a JEOL JXA-8230 Electron Probe Microanalyzer (EPMA) with four wavelength-dispersive spectrometers at the Center for Global Tectonics, School of Earth Sciences, China University of Geosciences (Wuhan). An accelerating voltage of 20 kV, a beam current of 20 nA, and a beam diameter of 1 µm were used for all the analyses. The dwell times were 10 s for the elemental peaks and 5 s for the background locations adjacent to the peaks. The following reference standards were used for calibration: SiO_2 (Si), TiO_2 (Ti), $NaAlSi_3O_8$ (Na and Al), Fe_2O_3 (Fe), $MnSiO_3$ (Mn), $(Mg,Fe)_2SiO_4$ (Mg), $CaCO_3$ (Ca), and $KAlSi_3O_8$ (K). The data were reduced online using the conventional ZAF routine. The analytical precision was >1% for elements with concentrations higher than 5 wt%, and better than 5% for elements with contents at 0.01–5 wt%. The structural formulas of tourmaline were calculated by normalizing to a sum of 15 cations in the octahedral and tetrahedral sites (T + Z + Y) following the method of Henry et al. (2011). The proportion of X-site vacancies was calculated as [1 – (Na + Ca + K)]. The B_2O_3 and H_2O contents were calculated from stoichiometric constraints, assuming B = 3 atoms per formula unit (apfu) and OH^- = 3.5 apfu. Mineral formulas were calculated assuming 31 total anions (O^{2-} and OH^-). The $Fe^{3+}/(Fe^{3+}+Fe^{2+})$ values of the tourmaline were estimated using the method described by Jiang et al. (2008). Despite the large uncertainties in the estimates, it has been shown to be useful in recording the relative oxidative-reductive conditions for successive tourmaline formations (Jiang et al. 2008; Zhao et al. 2021a).

The trace elemental compositions of the tourmaline were determined by laser ablation inductively coupled plasma mass spectrometry (LA-ICP-MS) at the State Key Laboratory of Geological Processes and Mineral Resources (GPMR), China University of Geosciences (Wuhan). A GeoLas 2005 laser ablation system coupled with an Agilent 7700 ICP-MS instrument was used. Laser sampling was performed with a spot size of 44 µm. A "wire" signal smoothing device was included in this laser ablation system, by which smooth signals were produced even at very low-laser repetition rates down to 1 Hz (Hu et al. 2012). Helium (~400 mL/min) was used as the carrier gas and mixed with argon (~800 mL/min) before entering the ICP system. A small amount of nitrogen (4 mL/min) was added to the central gas flow to enhance sensitivity, improve precision, and lower detection limit. Each analysis incorporated a background acquisition of ~20–30 s (gas blank), followed by 50 s of data acquisition from the sample. The data were calibrated against multiple reference standards: BIR-1G, BCR-2G, BHVO-2G, and SRM610. Raw data reduction was performed offline using ICPMSDataCal software (Liu et al. 2008), and quantitative calibration was performed using the method described by Chen et al. (2014). The analytical precision for most elements was estimated to be better than 10%.

The boron isotopes of tourmaline were analyzed using a RESOlution S-155 laser ablation system coupled to a Nu Plasma II multi-collector ICP-MS (LA-MC-ICP-MS) at the GPMR. The analyses were performed using a 50 µm diameter spot with a laser fluence of 4 J/cm^2 and a repetition frequency of 10 Hz. The isotopic signals of ^{10}B and ^{11}B were simultaneously acquired using two Faraday cups. The mass bias of the instrument was calibrated using the standard-sample-standard bracketing method. An international tourmaline standard IAEA B4 ($\delta^{11}B$ = –8.71‰; Tonarini et al. 2003) was used for external calibration. Two other tourmaline reference materials, schorl (HS#112566) and dravite (HS#108796) from the Harvard Mineralogical Museum (Dyar et al. 2001) were used to assess the analytical quality. The external precision (2σ) is estimated to be better than 0.5‰ based on replicate analyses of the reference tourmalines. The internal precision (1SD) in per mil for a single analysis was calculated from approximately 100 cycles of each analysis (Zhao et al. 2021b).

Results

Major element compositions

The major elemental compositions and structural formulas of the tourmaline samples are listed in Online Materials[1] Table A1 and graphically illustrated in Figure 6. Tourmaline samples from the different levels shared comparable SiO_2 (33.15–37.04%), B_2O_{3cal} (9.71–10.54%), and H_2O_{cal} (2.93–3.18%) concentrations (Fig. 6). However, notable variations were observed in the abundances of other oxides from the deep to shallow parts of the Hewan porphyry. For example, the median concentrations of FeO, MgO, Na_2O, and CaO in the tourmaline gradually increased from 510 to 1230 m a.s.l. (Fig. 6; Online Materials[1] Table A1). In contrast, the Al_2O_3 and K_2O concentrations of the tourmaline samples decreased from 510 to 1230 m a.s.l. (Fig. 6; Online Materials[1] Table A1). The median concentrations of TiO_2 and MnO in tourmaline showed more varied depth patterns, i.e., both increased from 510 to 830 m a.s.l. and then decreased to 1230 m a.s.l. (Fig. 6; Online Materials[1] Table A1). Tourmaline samples from 510 m a.s.l. yielded $Fe^{3+}/(Fe^{3+}+Fe^{2+})$ values of 0–0.16 (with a mean of 0.06). These values increased to 0–0.63 (mean = 0.17) and 0.16–0.80 (mean = 0.33) for tourmaline samples from 830 and 1230 m a.s.l., respectively (Online Materials[1] Table A1).

According to the classification by Henry et al. (2011), the studied tourmaline samples mostly belonged to the alkali group, although a few grains from 510 m a.s.l. plotted in the X-vacancy group (Fig. 7a). In the Al-Fe-Mg ternary diagram (Henry and Guidotti 1985), tourmaline samples from 510 m a.s.l. plotted in the fields of Li-poor granitoids and associated pegmatites and aplites, or metapelites and metapsammites without an Al-saturating phase (Fig. 7b). Similarly, samples from 830 m a.s.l. mainly plotted in these two fields, with a few scattered in the fields of Fe^{3+}-rich quartz-tourmaline rocks, calc-silicate rocks, or metapelites and metapsammites with an Al-saturating phase (Fig. 7b). However, samples from the shallowest 1230 m a.s.l. mostly plotted in the fields of Fe^{3+}-rich quartz-tourmaline rocks, calc-silicate rocks, and metapelites (Fig. 7b). The Mg/(Mg+Fe), Na/(Na+Ca) values, and X-site vacancies ($X_\square$) for the tourmaline samples showed some scatter with depth, but were most clearly plotted in the schorl field (Fig. 8).

The tourmaline samples showed varying and poorly defined trends in the Fe vs. Mg (Fig. 9a) diagram, suggesting composite

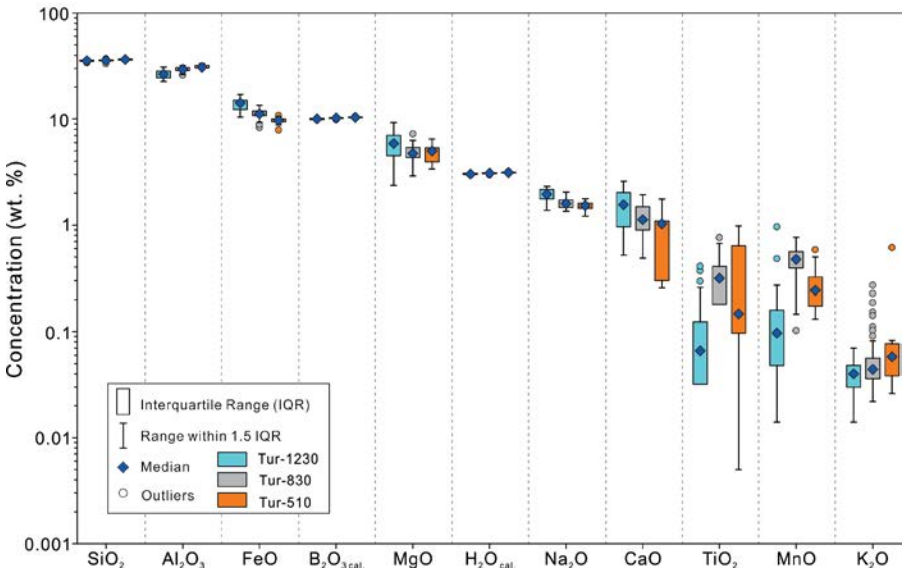

Figure 6. Box-whisker plot showing major elemental composition of tourmaline samples from 510 m (Tur-510), 830 m (Tur-830), and 1230 m (Tur-1230) a.s.l. of the Hewan porphyry. (Color online.)

substitutions including $FeMg_{-1}$, [(□,Al)$(Na,Mg)_{-1}$], and $FeAl_{-1}$ (e.g., Baksheev et al. 2018; Qiao et al. 2019). In the diagram of Al-$X_□$ vs. R+$X_□$ (Fig. 9b), all samples were plotted parallel to the $FeAl_{-1}$ exchange vector, which implies that Al variations in the tourmaline were dominantly controlled by $FeAl_{-1}$ substitution (Medaris et al. 2003; Henry et al. 2008). The negative correlation between Ca and $X_□$ (Fig. 9c) indicated {(Ca,R,O)[□,Al,(OH)]$_{-1}$} substitution for the investigated tourmaline samples. The correlations decreased for tourmaline from 510 to 1230 m a.s.l., suggesting an increasingly synergistic influence of [(Ca,R)$(Na,Al)_{-1}$] substitution from deep to shallow levels. Besides, the variations of Al (4.73–6.52 apfu) in these tourmaline samples were larger than that of Ca (0.05–0.48 apfu), further confirming that other exchange vectors, such as $FeAl_{-1}$ and [(R,OH)$(AlO)_{-1}$] operated to balance the excess Al (Fig. 9d).

For the oscillatory-zoned tourmaline grains at 1230 m a.s.l. (Fig. 10a), the Si, Fe, and Ca concentrations increased from the cores to the rims (Figs. 10b–10d). In contrast, the Al, B_2O_{3cal}, and H_2O_{cal} concentrations were relatively high in the cores and gradually decreased toward the rims (Figs. 10e–10g).

Trace element compositions

The trace element compositions of the tourmaline samples are listed in Online Materials[1] Table A2. The ranges and median values of individual elements are graphically shown in Figure 11. Most trace elements had concentrations ranging from 0.1 to tens of ppm. The highest median concentrations were those of V, Cr, Zn, Ga, and Sr, which varied from several tens to hundreds of ppm. In contrast, the concentrations of Cu, Ge, As, Rb, Y, Zr, Mo, Ag, Cd, Sb, Ba, Hf, Ta, W, Bi, Th, and U were mostly below 1 ppm or even below the detection limits. Numerous trace elements had concentrations that varied over several orders of magnitude, especially V, Cr, Co, Nb, Ta, Pb, Th, and U. Li, Co, Sr, Nb, and Sn concentrations in the tourmaline samples gradually increased

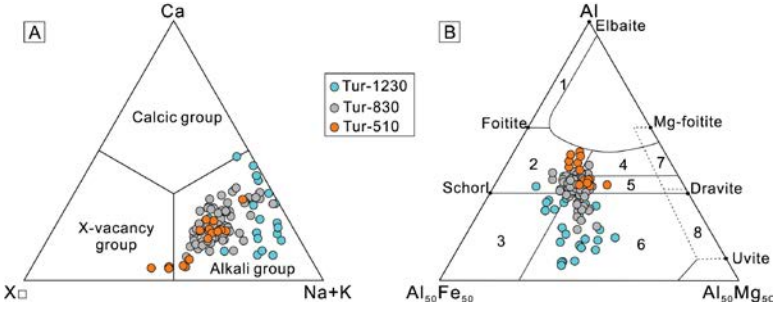

Figure 7. (**a**) Classification of the principal groups of tourmaline samples from 510 m (Tur-510), 830 m (Tur-830), and 1230 m (Tur-1230) a.s.l. of the Hewan porphyry (after Henry et al. 2011). $X_□$ = X-site vacancy. (**b**) Al-Fe-Mg ternary diagram showing tourmaline samples from the three different levels of the Hewan porphyry (after Henry and Guidotti 1985). 1 = Li-rich granitoid pegmatites and aplites; 2 = Li-poor granitoids and their associated pegmatites and aplites; 3 = Fe^{3+}-rich quartz-tourmaline rocks (hydrothermally altered granites); 4 = metapelites and metapsammites with an Al-saturated phase; 5 = metapelites and metapsammites without an Al-saturated phase; 6 = Fe^{3+}-rich quartz-tourmaline rocks, calc-silicate rocks, and metapelites; 7 = low-Ca metaultramafics and Cr,V-rich sediments; 8 = metacarbonates and metapyroxenites. (Color online.)

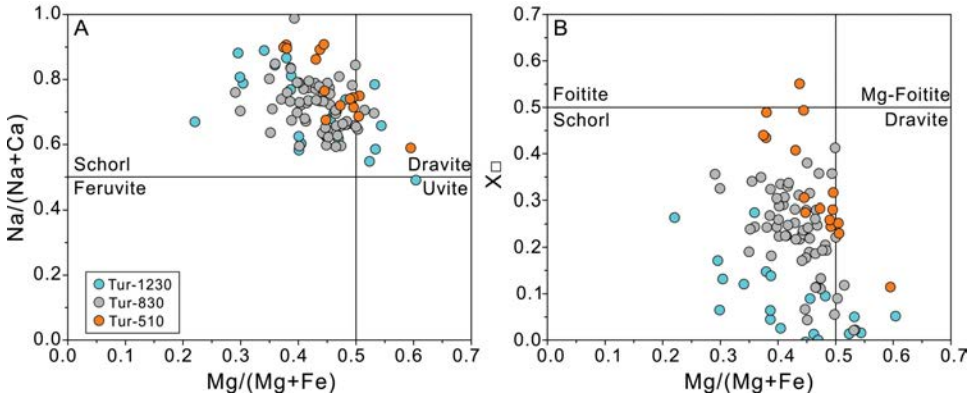

Figure 8. Plots of Mg/(Mg+Fe) vs. Na/(Na+Ca) (**a**) and Mg/(Mg+Fe) vs. X-site vacancy ($X_□$) (**b**) of tourmaline samples from 510 m (Tur-510), 830 m (Tur-830), and 1230 m (Tur-1230) a.s.l. of the Hewan porphyry. (Color online.)

from 510 to 1230 m a.s.l. In contrast, the Zn, Ta, Pb, Th, and U contents decreased (Figs. 11 and 12). Tourmaline samples generally had low REE contents, many of which were below the detection limits (Figs. 11 and 12i). The tourmaline samples from 510 m a.s.l. contained higher LREE with negligible HREE. In contrast, tourmaline samples from 830 and 1230 m a.s.l. were enriched in HREE relative to LREE (Online Materials[1] Table A2; Fig. 13). The median REE content of the tourmaline samples decreased from 510 to 1230 m a.s.l. (Figs. 11 and 12i).

Boron isotopic compositions

The boron isotopic compositions of the studied tourmaline samples are provided in Online Materials[1] Table A3 and are graphically illustrated in Figure 14. Tourmaline samples from 510 m a.s.l. had a tight $\delta^{11}B$ interval from –11.5 to –9.3‰, with a mean value of –10.3‰ (n = 16). The $\delta^{11}B$ values for tourmaline sampled from 830 m a.s.l. were higher than those from 510 m a.s.l., ranging from –9.9 to –1.5‰ (mean = –5.7‰; n = 64). Tourmaline samples from the shallowest level, 1230 m a.s.l., were characterized by the most

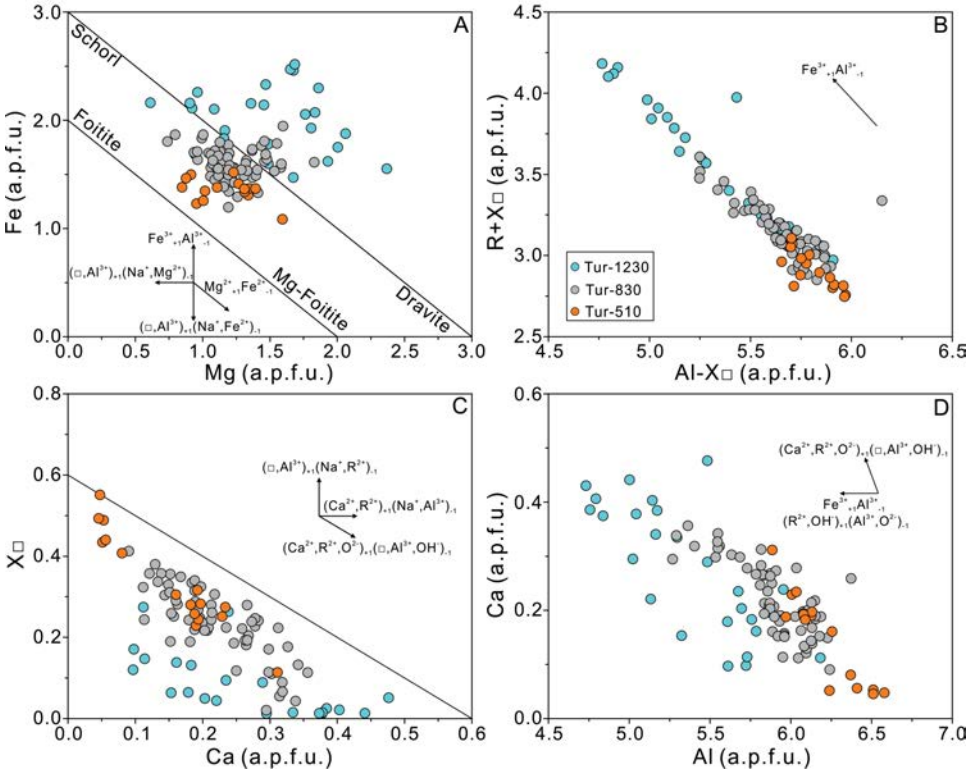

Figure 9. Plots of Mg vs. Fe **(a)**, Al-$X_□$ vs. R+$X_□$ **(b)**, Ca vs. $X_□$ **(c)**, and Al vs. Ca (**d**) of cation occupancies in tourmaline samples from 510 m (Tur-510), 830 m (Tur-830), and 1230 m (Tur-1230) a.s.l. of the Hewan porphyry. The common exchange vectors are also shown as references. $X_□$ = X-site vacancy; R = Fe+Mg+Mn; apfu = atoms per formula unit. (Color online.)

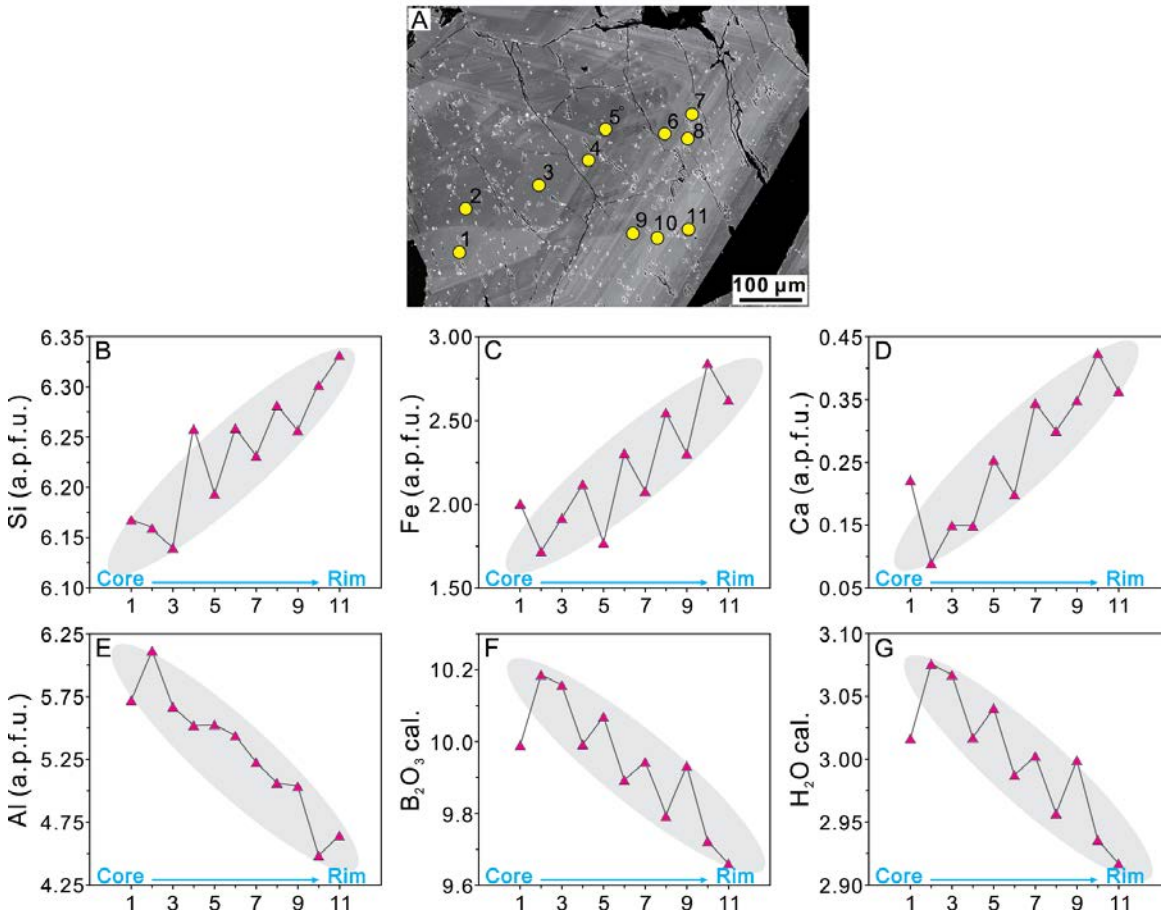

Figure 10. (**a**) The BSE image showing the oscillatory-zoned tourmaline from 1230 m a.s.l. of the Hewan porphyry. Also shown are the locations of EPMA analyses from core to rim. The analytical results of Si, Fe, Ca, and Al contents, and calculated B_2O_3 and H_2O contents against the locations are illustrated in **b**–**g**, respectively. (Color online.)

variable boron isotopic compositions, yielding $\delta^{11}B$ values in a range of –8.0 to +6.8‰ (–2.8‰; n = 25). Due to the small grain sizes, the internal $\delta^{11}B$ variations within individual tourmaline grains in the 510 m a.s.l. could not be obtained by LA-ICP-MS. The $\delta^{11}B$ values generally decreased from cores to rims for patchy tourmaline grains at 830 m a.s.l. (Fig. 4f) but broadly increased outward for oscillatory-zoned tourmaline grains at 1230 m a.s.l. (Fig. 5f). Collectively, the $\delta^{11}B$ values for all tourmaline samples ranged from –11.5 to +6.8‰ (Fig. 14).

Discussion

Tourmaline origin

Tourmaline samples from different levels of the Hewan porphyry coexisted spatially with quartz, pyrite, and other alteration minerals, which predominantly formed orbicules or patches that accounted for ~1% of the porphyry (Figs. 3–5). Similar tourmaline occurrences and mineral assemblages have been reported in leucocratic granitic rocks elsewhere, such as the Erongo granite in Namibia (Trumbull et al. 2008), the Heemskirk and Pieman Heads granites in western Tasmania, Australia (Hong et al. 2017), and the Pingying granite in South China (Zhao et al. 2021a). Three explanations have been proposed to understand the genesis of these tourmaline orbicules or patches: (1) formed through post-magmatic metasomatism by external boron-rich fluids (e.g., Rozendaal and Bruwer 1995); (2) direct crystallization from a B-rich granitic melt (e.g., Perugini and Poli 2007); and (3) precipitation from immiscible, aqueous, and boron-rich fluids during the late stages of granite crystallization (e.g., Trumbull et al. 2008; Balen and Petrinec 2011; Drivenes et al. 2015). The tourmaline orbicules and patches in the Hewan porphyry were physically isolated entities that were unrelated to fractures or veins connected to the enveloping wall rocks (Figs. 3–5). As such, we propose that the tourmaline orbicules and patches were not formed by post-magmatic metasomatism of external fluids. The tourmaline crystals and associated quartz in the orbicules commonly grew perpendicular to the matrix of the Hewan porphyry and replaced feldspar in the matrix (Figs. 3–5), suggesting that tourmaline formation occurred later than porphyry crystallization. Furthermore, the tourmaline grains were intimately intergrown with hydrothermal alteration minerals rather than with rock-forming minerals (Figs. 3–5). In addition, quartz contained abundant boiling fluid inclusion assemblages (Figs. 3d, 4d, and 5d). These combined lines of evidence indicate that the tourmaline grains in the Hewan porphyry predominantly

crystallized from exsolved, immiscible, aqueous, and boron-rich magmatic-hydrothermal fluids. This view was partly supported by the consistent age of Au mineralization and the hosting Hewan porphyry at ca. 140 Ma (Zhang et al. 2017, 2020).

Previous experimental and textural studies have suggested that crystallization may have caused the granitic magma to separate into aluminosilicate melts and hydrosaline fluids (Veksler et al. 2002; Thomas et al. 2003). During the separation process, K, Si, and Al are preferentially partitioned into the aluminosilicate melt, whereas B, Na, and Fe enter the hydrosaline fluid (Veksler and Thomas 2002; Veksler et al. 2002; Thomas et al. 2003). The ubiquitous leucocratic halos surrounding the tourmaline orbicules are generally represented by residual K-, Si-, and Al-rich melts after the separation of the B-, Na-, and Fe-rich fractions. In addition, because of the migration of Al into the aluminosilicate melt, the B-rich hydrosaline fluid is predicted to be Al-deficient (Thomas et al. 2003). The Al required for tourmaline growth generally originates from the metasomatism of adjacent feldspars and accounts for the intimate mineral associations of tourmaline, sericite, chlorite, smectite, and kaolinite, which are the replacement products of feldspar.

Although minor tourmaline samples at 830 m a.s.l. occurred as veins, they were isolated in the Hewan porphyry without any connection to the surrounding rocks (Fig. 4b). Furthermore, the tourmaline grains in the veins had morphologies, textures, mineral assemblages, and chemical compositions indistinguishable from those in the orbicules (Online Materials[1] Tables A1–A3). These features suggest that the tourmaline crystals in the veins and orbicules shared a similar origin and that they precipitated from an immiscible, hydrosaline, and B-rich fluid during the late evolution of the Hewan porphyry. Similar tourmaline occurrences have been identified in numerous granitoid intrusions in Tasmania, Australia, and South China (Yang et al. 2015; Hong et al. 2020; Zhao et al. 2021b). A likely explanation for the different tourmaline occurrences is that the tourmaline veins formed later than the orbicules/patches, and the associated fractures provided conduits for migration of the B-rich hydrosaline fluids (e.g., Hong et al. 2020). Collectively, the above textural and petrographic observations suggest that the tourmaline samples from different parts of the Hewan porphyry crystallized predominately from the magmatic-hydrothermal fluids.

Records of hydrothermal fluid evolution

Previous studies have shown that the composition of hydrothermal tourmaline is controlled not only by crystallogra-phy (e.g., Marks et al. 2013) but also by geochemistry of the fluids (e.g., Jiang et al. 2002, 2008; Slack and Trumbull 2011) chemical composition of the host rocks (e.g., Henry and Guidotti 1985; Su et al. 2016), and pressure-temperature conditions (e.g., von Goerne et al. 2001, 2011; Berryman et al. 2015). Therefore,

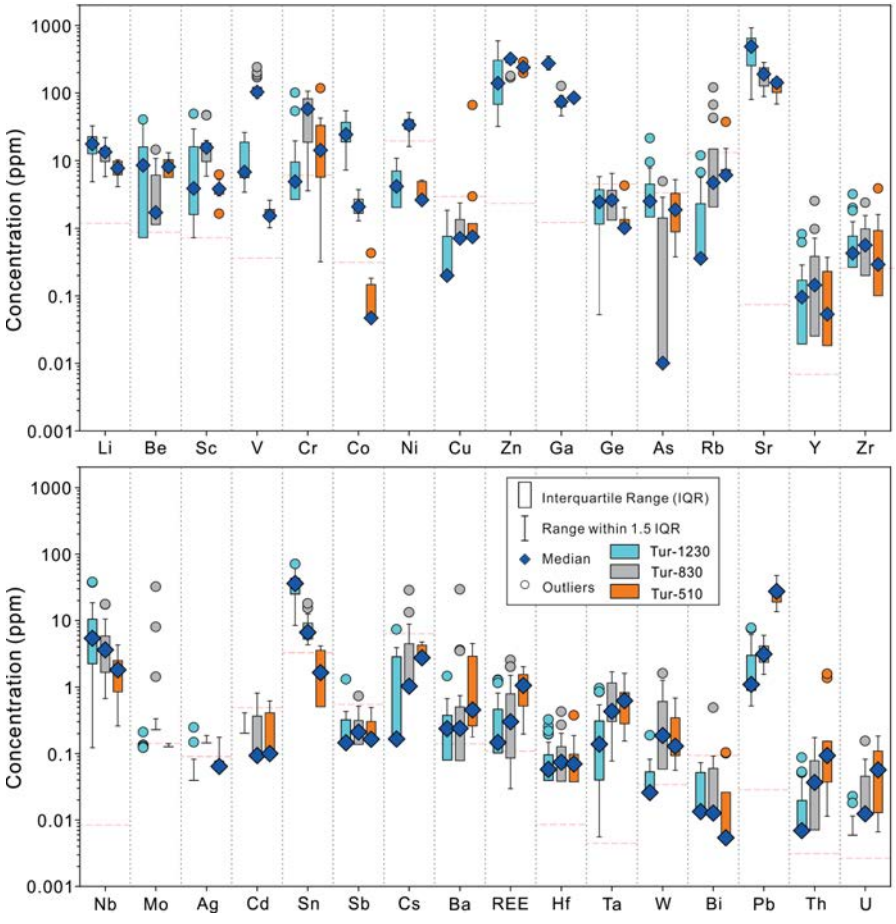

Figure 11. Box-whisker plot showing trace elemental compositions of tourmaline samples from 510 m (Tur-510), 830 m (Tur-830), and 1230 m (Tur-1230) a.s.l. of the Hewan porphyry. (Color online.)

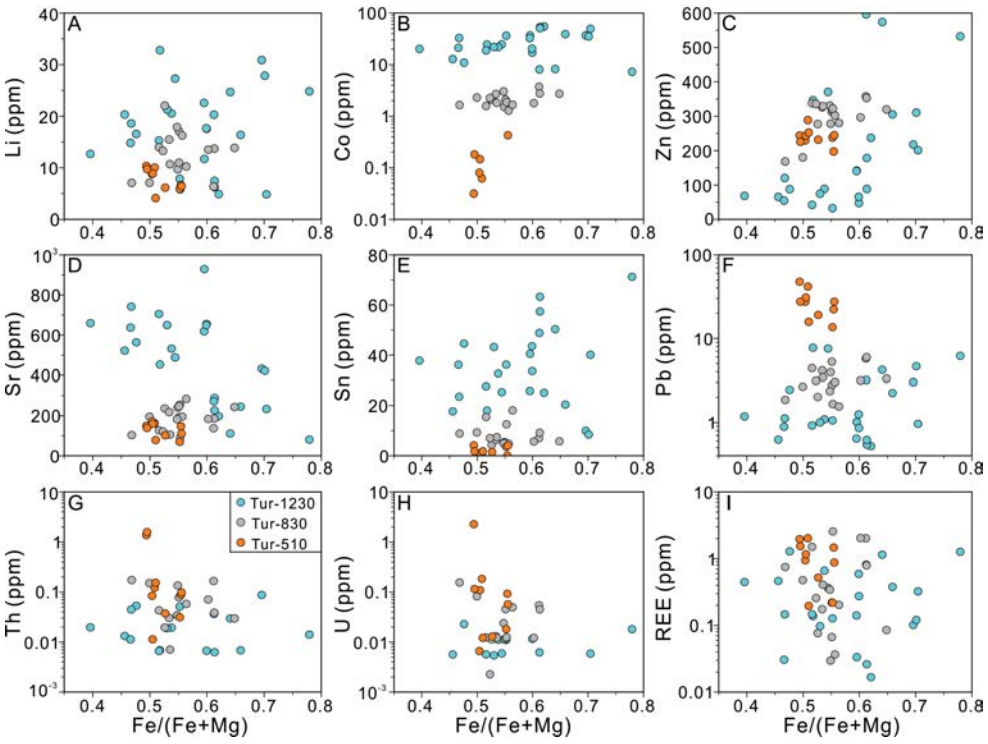

Figure 12. Correlation diagrams of Li (**a**), Co (**b**), Zn (**c**), Sr (**d**), Sn (**e**), Pb (**f**), Th (**g**), U (**h**), and REE (**i**) contents against Fe/(Mg+Fe) value for tourmaline samples from 510 m (Tur-510), 830 m (Tur-830), and 1230 m (Tur-1230) a.s.l. of the Hewan porphyry. (Color online.)

elements with few crystal effects can be used to investigate the associated geological processes that control the evolution of tourmaline chemistry. Major and trace element correlations are commonly used to reveal the dominant factors controlling tourmaline composition (e.g., Marks et al. 2013; Zhao et al. 2019, 2021a). In this study, almost all the trace elements (e.g., Li, Co, Zn, Sr, Sn, Pb, Th, U, and REE) showed no statistical correlations with Fe/(Fe+Mg) (Fig. 12), suggesting that they were controlled by external factors such as fluid composition and local fluid-rock interaction as previously proposed (e.g., Yang et al. 2015; Duchoslav et al. 2017; Kalliomäki et al. 2017).

From the deep to shallow parts of the Hewan porphyry, the Fe content of tourmaline increased, whereas the Al content decreased (Fig. 6). Similar Fe and Al variations were observed from the cores to the rims of the oscillatory-zoned tourmaline grains in the shallowest part of the porphyry (Fig. 10). The variations in Fe and Al concentrations, combined with the $FeAl_{-1}$ exchange vector (Fig. 9) and increasing tourmaline $Fe^{3+}/(Fe^{3+}+Fe^{2+})$ values from deep to shallow parts (Online Materials[1] Table A1), generally suggest an increasing oxygen fugacity from 510 to 1230 m a.s.l. and from cores to rims of the zoned tourmaline grains at 1230 m a.s.l., which could promote the incorporation of Fe into tourmaline (e.g., Zhao et al. 2021a). This gradual increase in oxygen fugacity was presumably induced by the injection of meteoric water, which commonly contains high levels of free oxygen (e.g., Fan et al. 1994; Zhao et al. 2021a). Convective meteoric water could have leached components from the peripheral Archean metamorphosed mafic volcanic rocks and Mesoproterozoic marine sedimentary rocks, resulting in gradually increasing concentrations of MgO, Na_2O, CaO, Li, Co, and Sr for tourmaline samples from 510 to 1230 m a.s.l. and from cores to rims of the zoned tourmaline grains at 1230 m a.s.l. (Figs. 6 and 10–12). The changing redox conditions and fluid mixing could also result in the removal of Sn from the hydrothermal fluid (e.g., Heinrich 1990; Zhao et al. 2021a), thus increasing the Sn concentration in the tourmaline samples from deep to shallow levels (Fig. 12e). A gradual change was observed in the composition from schorl to dravite for tourmaline samples from the deep to shallow parts of the Hewan porphyry (Fig. 8). This has been experimentally interpreted in terms of the increasing salinity of the source fluids for tourmaline crystallization (von Goerne et al. 2011; Orlando et al. 2017). This salinity increase was likely caused by the contamination of leached materials from Mesoproterozoic marine carbonates and evaporites through the circulation of meteoric water. Another possibility is that the wall rock contamination added extra Mg, as addressed above, to the hydrothermal system, which could also contribute to the tourmaline compositional shift from schorl to dravite from deep to shallow parts.

In contrast, the median U, Th, REE, Zn, and Pb contents of the tourmaline samples gradually decreased from 510 to 1230 m a.s.l. (Figs. 11 and 12). Furthermore, the tourmaline grains sampled from 510 m a.s.l. were enriched in LREE relative to HREE, whereas those from 830 and 1230 m a.s.l. contained lower LREE than HREE (Fig. 13). Tourmaline samples of 510 m a.s.l. yielded chondrite-normalized REE patterns consistent with the host Hewan porphyry (Zhang et al. 2017), which reflect the magmatic fractionation of zircon, monazite, and apatite in the peraluminous melt (e.g., Pettke et al. 2005). Similar REE features have been identified for tourmaline in numerous magmatic-hydrothermal systems (e.g., Jiang et al. 2004; Yang et al. 2015; Duchoslav et al. 2017) and are commonly interpreted to reflect preferential partitioning of LREE into the magmatic-hydrothermal fluids exsolved from peraluminous granitic melts (Reed et al. 2000). This feature partly confirms that the tourmaline grains at 510 m a.s.l.

precipitated from the hydrothermal fluid that evolved from the Hewan porphyry. Several processes can explain the above vertical variations of REE concentrations and chondrite-normalized REE patterns of the tourmaline samples: (1) the presence of HREE-rich mineral inclusions in the tourmaline; (2) co-crystallization of LREE-incorporating phases (e.g., garnet, monazite, apatite) during fluid evolution and tourmaline precipitation; (3) fluid-rock interactions or fluid mixing resulting in fractionation of LREE and HREE (e.g., Jiang et al. 2004; Marks et al. 2013; Yang et al. 2015; Harlaux et al. 2020). The first hypothesis is unlikely because significant caution was taken to screen out any contamination from accessory mineral inclusions in the tourmaline during data processing. Furthermore, even if some tiny accessory minerals were hidden below the tourmaline surface, ablating trace amounts of such accessories may significantly increase the HREE content as well as the total REE content (e.g., Jiang et al. 2004; Yang et al. 2015), which is not consistent with

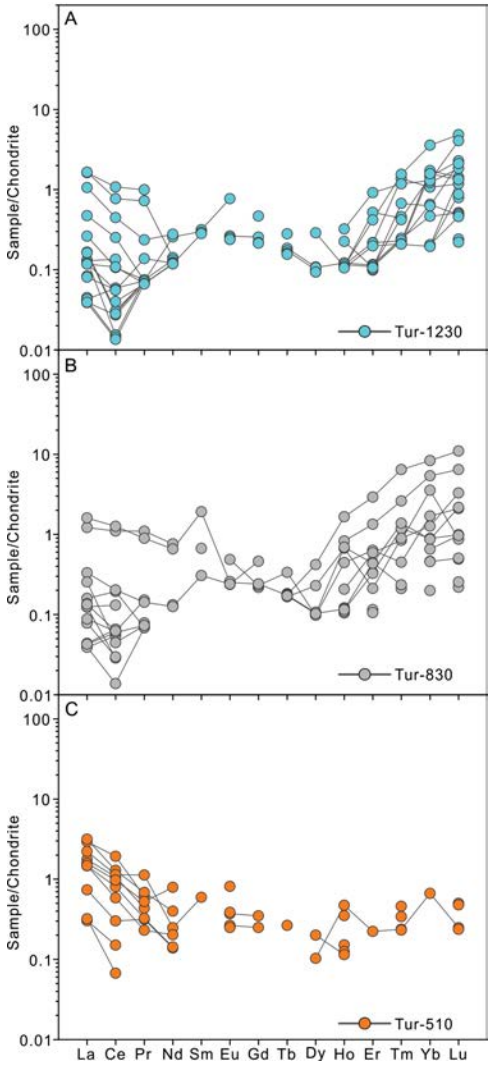

Figure 13. Chondrite-normalized REE patterns for tourmaline from 1230 m (Tur-1230), 830 m (Tur-830), and 510 m (Tur-510) a.s.l. of the Hewan porphyry. The C1 chondrite data are referred from Sun and McDonough (1989). (Color online.)

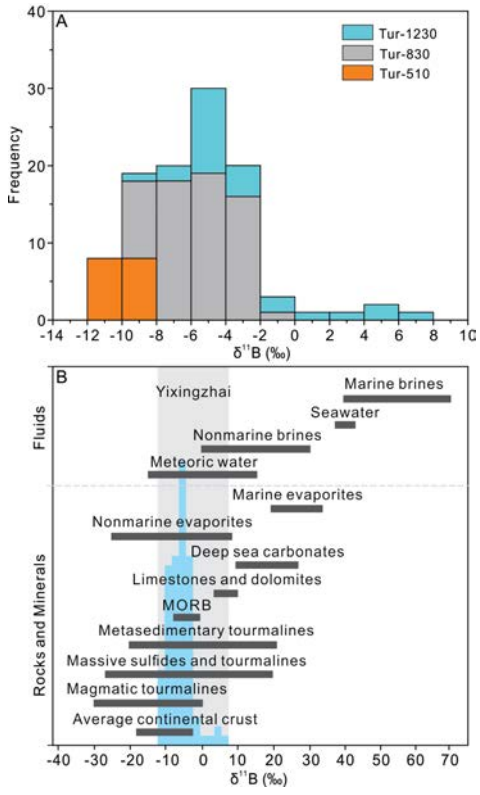

Figure 14. (**a**) Histogram of $\delta^{11}B$ values of tourmaline samples from 510 m (Tur-510), 830 m (Tur-830), and 1230 m (Tur-1230) a.s.l. of the Hewan porphyry. (**b**) Distribution of $\delta^{11}B$ values of several boron reservoirs (Jiang and Palmer 1998; Marschall and Jiang 2011; Mercadier et al. 2012). (Color online.)

the observed decrease in the total REE content from LREE-rich tourmaline to HREE-rich tourmaline (Figs. 12i and 13). The second hypothesis is a likely explanation for the variation in the tourmaline REE patterns because previous studies have revealed the presence of LREE-rich hydrothermal garnet (Zhang et al. 2020). These garnet grains may have sequestered more LREE than HREE during fluid evolution, resulting in tourmaline at shallower levels containing lower REE concentrations and showing relative HREE enrichment. The third hypothesis may also be involved in REE fractionation. In hydrothermal systems, REE can be complexed with various ligands such as Cl^-, CO_3^{2-}, and F^- (e.g., Wood 1990; Bau 1991; Jiang et al. 1997; Migdisov et al. 2016). The LREE complexes are more stable and mobile than HREE complexes, and this difference in stability increases with increasing temperature (Wood 1990; Migdisov et al. 2016). As such, fluid mixing between magmatic-hydrothermal fluid and meteoric water in the shallower parts of the Hewan porphyry, as revealed by the above major-trace elements, would result in the fractionation of HREE compared to the more mobile LREE in the fluid and subsequent precipitation of HREE-rich tourmaline.

The decreasing Zn and Pb concentrations from the deep to shallow parts were consistent with the distribution of the Au grade (Fig. 2), suggesting that sphalerite and galena co-precipitated with Au-bearing pyrite mainly at deep levels, resulting in the gradual depletion of the residual fluid in these elements. This

view is consistent with the mineral assemblages described in the "Geological background" section. Therefore, the major and trace elemental compositions of the tourmaline indicated that the exsolved magmatic-hydrothermal fluid played a dominant role in the deeper parts of the Hewan porphyry. The fluid migrated upward and gradually mixed with external meteoric water containing materials leached from Archean metamorphic rocks and Mesoproterozoic marine sedimentary rocks at shallower levels. Au, Pb, and Zn were predominantly deposited in the deeper parts (e.g., 510 and 830 m a.s.l.).

Constraints on the source of ore fluids

Tourmaline samples from the deepest 510 m a.s.l. yielded a tight $\delta^{11}B$ interval from –11.5 to –9.3‰ (Fig. 14a), which is consistent with $\delta^{11}B$ values of the average continental crust (Fig. 14b) and tourmaline formed in magmatic systems (–15 to –5‰; Marschall and Jiang 2011). This boron isotopic comparability suggests that the boron for the tourmaline samples at 510 m a.s.l. was predominately sourced from the Hewan porphyry, which was mainly derived from the lower crust, as demonstrated by the major and trace element geochemistry and Sr-Nd-Pb isotopes (Zhang et al. 2017). Tourmaline samples from 830 and 1230 m a.s.l. yielded higher $\delta^{11}B$ values of –9.9 to –1.5‰ and –8.0 to +6.8‰, respectively (Fig. 14a). The increasing tourmaline $\delta^{11}B$ values from deep to shallow parts were consistent with boron isotopic variations from cores to rims of the oscillatory-zoned tourmaline in the shallowest level (Fig. 5f). These boron isotopic shifts could have been resulted from (1) the fractionation of boron in the ore fluids of a closed system (i.e., phase separation, Rayleigh fractionation) and/or (2) the mixing of boron from multiple reservoirs in an open system (Krienitz et al. 2008; Pal et al. 2010; Trumbull et al. 2013).

Quartz grains intergrown with tourmaline at different levels contained similar fluid inclusion assemblages comprising single-phase liquid, two-phase vapor-liquid, and three-phase halite-bearing fluid inclusions (Figs. 3d, 4d, and 5d), suggesting that phase separation occurred during the alteration and mineralization of the Hewan porphyry. Previous studies, however, have shown that $\Delta^{11}B_{vapor\text{-}liquid}$ are very small (<3‰) at temperatures higher than 140 °C (Spivack et al. 1990; Leeman et al. 2005; Liebscher et al. 2005), which cannot account for the largely variable boron isotopes observed here (Fig. 14). Nevertheless, this process could be locally responsible for the decreasing $\delta^{11}B$ values from cores to rims within tourmaline grains (e.g., Fig. 4f). Therefore, in this study, we precluded the possibility of phase separation as the dominant control for boron isotopic variation.

Rayleigh fractionation is another significant mechanism that causes boron isotopic shifts in tourmaline. To better evaluate the role of this process in the observed boron isotopic variation, we used model calculations (Fig. 15). The $\Delta^{11}B_{liquid\text{-}tourmalie}$ is 3.8‰ (Meyer et al. 2008) at 300 °C, the peak homogenization temperature of fluid inclusions in quartz of the main Au mineralization stage (Lu et al. 2012; Peng et al. 2017). The starting $\delta^{11}B$ value of ore fluid (–7.7‰) was calculated using the lowest $\delta^{11}B$ value of tourmaline (–11.5‰) in this study. The model shows that the percentage of initial boron in the residual fluid (F value) should be less than 0.07 for the boron isotopic composition of tourmaline samples at 830 m a.s.l. (Fig. 15). Such an extreme fractionation is geologically unlikely because of the high-modal proportion of

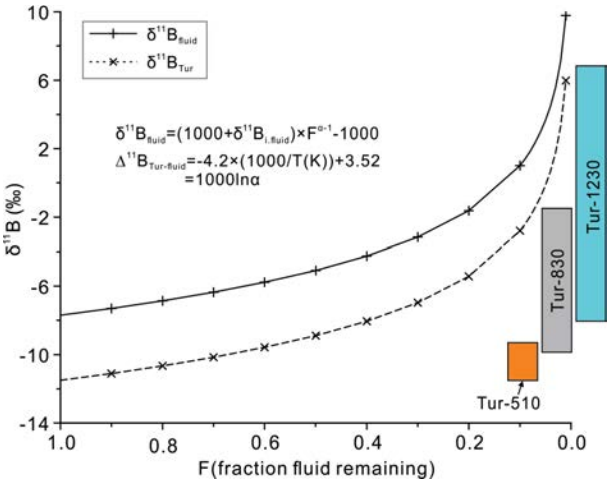

Figure 15. Rayleigh fractionation model on the evolution of tourmaline and equilibrated fluid $\delta^{11}B$ values in the Hewan porphyry. Tourmaline samples from 510 m, 830 m, and 1230 m a.s.l. of the Hewan porphyry are termed as Tur-510, Tur-830, and Tur-1230, respectively. See the text for details. (Color online.)

tourmaline in the samples. In addition, Rayleigh fractionation could not account for the most positive boron isotopic values of the tourmaline samples at the shallowest level (Fig. 15). Therefore, Rayleigh fractionation was neither the major nor the only process that caused the observed boron isotopic variation.

Collectively, boron mixing from two reservoirs, one with an enrichment of ^{10}B, represented by the Hewan porphyry, and the other by an external reservoir typically enriched in ^{11}B, is the most likely explanation for the observed boron isotopic variation (e.g., Li et al. 2022). The potential reservoirs rich in ^{11}B are rocks/fluids of marine origin, including marine brine, seawater, marine evaporites, and deep-sea carbonates (Fig. 14b). Marine brine and seawater are unlikely because the adjacent paleo oceans closed at least 100 Ma earlier than Au mineralization (e.g., Zhao et al. 2005; Zhang et al. 2020; Wu et al. 2021). Mesoproterozoic dolomites and marbles containing marine evaporites were locally present in the Yixingzhai Au mine, particularly in the Hewan porphyry (Fig. 1). As such, we propose that boron in the marine sedimentary rocks, presumably leached and incorporated by convective meteoric water, caused the increasing $\delta^{11}B$ values from deep to shallow levels (e.g., Xavier et al. 2008).

Implications

Au deposition and further exploration

As documented in the "Geological background" section, gold in the mineralized Hewan porphyry mainly occurs as native Au or electrum inclusions in pyrite, which are closely associated with alteration minerals such as quartz, sericite, chlorite, and tourmaline. However, the presence of these alteration minerals does not always indicate the location of economic Au ores, which are predominantly distributed between 500 and 1100 m a.s.l. in the Hewan porphyry (Fig. 2). Clarifying the mechanisms of Au precipitation and chemical proxies for economic zones is essential for revealing the genesis of the Au mineralization and for further Au exploration. In magmatic-hydrothermal ore systems, metal precipitation

is commonly caused by fluid separation, fluid-rock interactions, and/or fluid mixing (e.g., Williams-Jones and Heinrich 2005; Sillitoe 2010; Fan et al. 2022). As recorded by the quartz fluid inclusion assemblages (Figs. 3d, 4d, and 5d), ore-forming fluid separation occurred during Au mineralization and associated alteration from 510 to 1230 m a.s.l. in the Hewan porphyry. However, only the zones between 500 and 1100 m a.s.l. contained large tonnages of high-grade Au ore (Fig. 2), which suggests that fluid separation was not the main mechanism for Au deposition. Nor was fluid-rock interaction the cause of ore deposition because ore-related alteration typically occupies larger spaces than the associated economic Au ores, and not all altered zones are accompanied by economic Au mineralization. The major-trace element and boron isotopic compositions of the tourmaline samples from variable levels of the Hewan porphyry suggest that boron and other metals and volatiles, by inference, were initially sourced from the Hewan porphyry and gradually mixed with meteoric water at shallower levels. As such, we propose that fluid mixing was likely the main mechanism for Au precipitation, although fluid separation and fluid-rock interactions may also locally contribute to the Au deposition. However, external contributions from the Archean metamorphic rocks and Mesoproterozoic marine sedimentary rocks were dominant at 1230 m a.s.l., which decreased with increasing depth to Au-rich 830 and 510 m a.s.l. This observation indicates that a suitable mixing proportion of metal-bearing magmatic-hydrothermal fluid and meteoric water accounted for the Au deposition. However, an accurate proportion could not be determined here and can be evaluated in further studies.

From deep to shallow parts of the Hewan porphyry, positive or negative correlations were observed between the $\delta^{11}B$ values and Co, Sr, Pb, and Zn contents of the tourmaline samples (Figs. 16a–16d). For example, $\delta^{11}B$ values of the tourmaline and its Co, Sr contents systematically increased, whereas Pb, Zn contents decreased from high-grade Au ores upwards to low-grade or barren zones. These systematic variations, combined

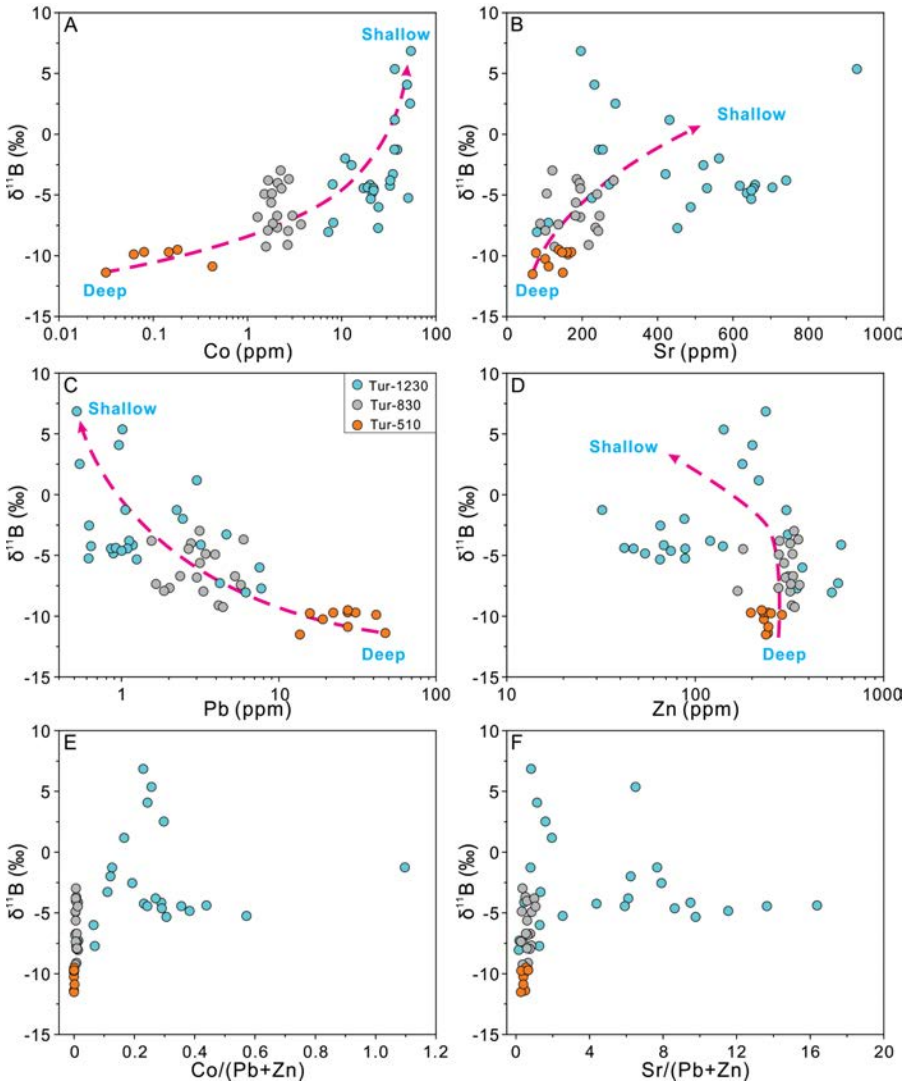

Figure 16. Binary plots of Co vs. $\delta^{11}B$ (**a**), Sr vs. $\delta^{11}B$ (**b**), Pb vs. $\delta^{11}B$ (**c**), Zn vs. $\delta^{11}B$ (**d**), Co/(Pb+Zn) vs. $\delta^{11}B$ (**e**), and Sr/(Pb+Zn) vs. $\delta^{11}B$ (**f**) for tourmaline samples from 510 m (Tur-510), 830 m (Tur-830), and 1230 m (Tur-1230) a.s.l. of the Hewan porphyry. (Color online.)

with the distribution of Au grade, suggest that tourmaline boron isotopes and trace element compositions could potentially act as proxies for Au exploration. Notably, the tourmaline samples from high-grade ore zones showed $\delta^{11}B$ (–11.5 to –3.0‰), Co/(Pb+Zn) (<0.01), and Sr/(Pb+Zn) (0.27–1.07) values much lower and more concentrated than those from low-grade or barren zone (–8.0 to +6.8‰, 0.01–1.10, 0.15–16.4, respectively; Figs. 16e–16f). As discussed above, cobalt and Sr in the tourmaline were predominantly derived from Archean to Mesoproterozoic rocks. In contrast, lead and Zn were mainly sourced from the Hewan porphyry and precipitated with Au. Therefore, the lower and more concentrated $\delta^{11}B$, Co/(Pb+Zn), and Sr/(Pb+Zn) values of tourmaline indicated a dominant magmatic provenance from the Hewan porphyry with minor external contaminations. Such fluids and zones, where tourmaline and pyrite precipitated, were favorable for Au accumulation to form economic ores (e.g., 510 and 830 m a.s.l. in Fig. 2). The increasing and largely scattered values of the three parameters suggested significant contamination from the Archean to Mesoproterozoic rocks by circulating meteoric water, which likely diluted Au and related elements in the ore-forming fluids, resulting in low-grade or even barren zones (e.g., 1230 m a.s.l. in Fig. 2). As such, the tourmaline $\delta^{11}B$, Co/(Pb+Zn), and Sr/(Pb+Zn) values could be useful proxies for exploring similar Au mineralization in the Yixingzhai gold mine. In addition to the mineralized Hewan body, other coeval plutons and cryptoexplosive breccia pipes are also present in the mine (Fig. 1b). Field investigations and independent studies have shown that tourmaline is widespread in these plutons and pipes (e.g., Li and Li 1997; Luo 2009; Li et al. 2014). Therefore, the chemical and isotopic proxies of tourmaline obtained in this study can potentially assist in further Au exploration and evaluation within and around these plutons and pipes.

Acknowledgments and Funding

We thank Guo-Ping Wang from the Mineral Exploration Institute, Zijin Mining Group Co., Ltd., and Jie Lin from the GPMR for their assistance during the field investigation and lab analyses. We also thank two anonymous reviewers for their constructive comments, which helped improve the presentation of the manuscript. We extend our gratitude to Don R. Baker and Fang-Zhen Teng for handling the manuscript. This research was funded by the MOST Special Fund from the GPMR of the China University of Geosciences (Wuhan) (MSFGPMR2022-5).

References cited

Arif, M., Henry, D.J., and Moon, C.J. (2010) Cr-bearing tourmaline associated with emerald deposits from Swat, NW Pakistan: Genesis and its exploration significance. American Mineralogist, 95, 799–809, https://doi.org/10.2138/am.2010.3349.

Baksheev, I.A., Trumbull, R.B., Popov, M.P., Erokhin, Y.V., Kudryavtseva, O.E., Yapaskurt, V.O., Khiller, V.V., Vovna, G.M., and Kiselev, V.I. (2018) Chemical and boron isotopic composition of tourmaline from the Mariinsky emerald deposit, Central Urals, Russia. Mineralium Deposita, 53, 565–583, https://doi.org/10.1007/s00126-017-0759-z.

Balen, D. and Petrinec, Z. (2011) Contrasting tourmaline types from peraluminous granites: A case study from Moslavačka Gora (Croatia). Mineralogy and Petrology, 102, 117–134, https://doi.org/10.1007/s00710-011-0164-8.

Bau, M. (1991) Rare-earth element mobility during hydrothermal and metamorphic fluid-rock interaction and the significance of the oxidation state of europium. Chemical Geology, 93, 219–230, https://doi.org/10.1016/0009-2541(91)90115-8.

Berryman, E.J., Wunder, B., Wirth, R., Rhede, D., Schettler, G., Franz, G., and Heinrich, W. (2015) An experimental study on K and Na incorporation in dravitic tourmaline and insight into the origin of diamondiferous tourmaline from the Kokchetav Massif, Kazakhstan. Contributions to Mineralogy and Petrology, 169, 28, https://doi.org/10.1007/s00410-015-1116-9.

Chen, C.F., Liu, X.G., Hu, Z.C., Zong, K.Q., and Liu, Y.S. (2014) In situ analysis of major and trace element compositions of hydrous silicate minerals by LA-ICP-MS. Earth Science, 39, 525–536 (in Chinese).

Drivenes, K., Larsen, R.B., Müller, A., Sørensen, B.E., Wiedenbeck, M., and Raanes, M.P. (2015) Late-magmatic immiscibility during batholith formation: Assessment of B isotopes and trace elements in tourmaline from the Land's End granite, SW England. Contributions to Mineralogy and Petrology, 169, 56, https://doi.org/10.1007/s00410-015-1151-6.

Duchoslav, M., Marks, M.A.W., Drost, K., McCammon, C., Marschall, H.R., Wenzel, T., and Markl, G. (2017) Changes in tourmaline composition during magmatic and hydrothermal processes leading to tin-ore deposition: The Cornubian Batholith, SW England. Ore Geology Reviews, 83, 215–234, https://doi.org/10.1016/j.oregeorev.2016.11.012.

Dutrow, B.L. and Henry, D.J. (2011) Tourmaline: A geologic DVD. Elements, 7, 301–306, https://doi.org/10.2113/gselements.7.5.301.

Dyar, M.D., Wiedenbeck, M., Robertson, D., Cross, L.R., Delaney, J.S., Ferguson, K., Francis, C.A., Grew, E.S., Guidotti, C.V., Hervig, R.L., and others. (2001) Reference minerals for the microanalysis of light elements. Geostandards Newsletter, 25, 441–463, https://doi.org/10.1111/j.1751-908X.2001.tb00616.x.

Fan, H.R., Xie, Y.H., Zhao, R., and Wang, Y.L. (1994) Stable isotope geochemistry of rocks and gold deposits in the Xiong'ershan area, western He'nan province. Contributions to Geology and Mineral Resources Research, 9, 54–64 (in Chinese).

Fan, G.H., Li, J.W., Valley, J.W., Scicchitano, M.R., Brown, P.E., Yang, J.H., Robinson, P.T., Deng, X.D., Wu, Y.F., Li, Z.K., and others. (2022) Garnet secondary ion mass spectrometry oxygen isotopes reveal crucial roles of pulsed magmatic fluid and its mixing with meteoric water in lode gold genesis. Proceedings of the National Academy of Sciences of the United States of America, 119, e2116380119, https://doi.org/10.1073/pnas.2116380119.

Gao, W.S. (2024) The lifespan and genesis of Yixingzhai gold deposit, Central Taihangshan District, 246 p. Ph.D. thesis, China University of Geosciences (Wuhan) (in Chinese).

Harlaux, M., Kouzmanov, K., Gialli, S., Laurent, O., Rielli, A., Dini, A., Chauvet, A., Menzies, A., Kalinaj, M., and Fontboté, L. (2020) Tourmaline as a tracer of late-magmatic to hydrothermal fluid evolution: The world-class San Rafael tin (-copper) deposit, Peru. Economic Geology and the Bulletin of the Society of Economic Geologists, 115, 1665–1697, https://doi.org/10.5382/econgeo.4762.

Harlaux, M., Kouzmanov, K., Gialli, S., Marger, K., Bouvier, A., Baumgartner, L.P., Rielli, A., Dini, A., Chauvet, A., Kalinaj, M., and others. (2021) Fluid mixing as primary trigger for cassiterite deposition: Evidence from in situ $\delta^{18}O$-$\delta^{11}B$ analysis of tourmaline from the world-class San Rafael tin (-copper) deposit, Peru. Earth and Planetary Science Letters, 563, 116889, https://doi.org/10.1016/j.epsl.2021.116889.

He, H. (2014) Enlightenment on geological characteristics and reserve verification of the Yixingzhai gold deposit in Shanxi Province. Huabei Land and Resources, 59, 123–125 (in Chinese).

Heinrich, C.A. (1990) The chemistry of hydrothermal tin(-tungsten) ore deposition. Economic Geology and the Bulletin of the Society of Economic Geologists, 85, 457–481, https://doi.org/10.2113/gsecongeo.85.3.457.

Henry, D.J. and Guidotti, C.V. (1985) Tourmaline as a petrogenetic indicator mineral—An example from the staurolite-grade metapelites of NW Maine. American Mineralogist, 70, 1–15.

Henry, D.J., Sun, H., Slack, J.F., and Dutrow, B.L. (2008) Tourmaline in metaevaporites and highly magnesian rocks: Perspectives from Namibian tourmalinites. European Journal of Mineralogy, 20, 889–904, https://doi.org/10.1127/0935-1221/2008/0020-1879.

Henry, D.J., Novák, M., Hawthorne, F.C., Ertl, A., Dutrow, B.L., Uher, P., and Pezzotta, F. (2011) Nomenclature of the tourmaline-supergroup minerals. American Mineralogist, 96, 895–913, https://doi.org/10.2138/am.2011.3636.

Hong, W., Cooke, D.R., Zhang, L., Fox, N., and Thompson, J. (2017) Tourmaline-rich features in the Heemskirk and Pieman Heads granites from western Tasmania, Australia: Characteristics, origins, and implications for tin mineralization. American Mineralogist, 102, 876–899, https://doi.org/10.2138/am-2017-5838.

Hong, W., Fox, N., Cooke, D.R., Zhang, L., and Fayek, M. (2020) B- and O-isotopic compositions of tourmaline constrain late-stage magmatic volatile exsolution in Tasmanian tin-related granite systems. Mineralium Deposita, 55, 63–78, https://doi.org/10.1007/s00126-019-00885-5.

Hu, Z.C., Liu, Y.S., Gao, S., Xiao, S.Q., Zhao, L.S., Günther, D., Li, M., Zhang, W., and Zong, K.Q. (2012) A "wire" signal smoothing device for laser ablation inductively coupled plasma mass spectrometry analysis. Spectrochimica Acta. Part B, Atomic Spectroscopy, 78, 50–57, https://doi.org/10.1016/j.sab.2012.09.007.

Jiang, S.Y. and Palmer, M.R. (1998) Boron isotope systematics of tourmaline from granites and pegmatites: A synthesis. European Journal of Mineralogy, 10, 1253–1266, https://doi.org/10.1127/ejm/10/6/1253.

Jiang, S.Y., Palmer, M.R., Peng, Q.M., and Yang, J.H. (1997) Chemical and stable isotopic compositions of Proterozoic metamorphosed evaporites and associated tourmalines from the Houxianyu borate deposit, eastern Liaoning, China. Chemical Geology, 135, 189–211, https://doi.org/10.1016/S0009-2541(96)00115-5.

Jiang, S.Y., Palmer, M.R., and Yeats, C.J. (2002) Chemical and boron isotopic

compositions of tourmaline from the Archean Big Bell and Mount Gibson gold deposits, Murchison Province, Yilgarn Craton, Western Australia. Chemical Geology, 188, 229–247, https://doi.org/10.1016/S0009-2541(02)00107-9.

Jiang, S.Y., Yu, J.M., and Lu, J.J. (2004) Trace and rare-earth element geochemistry in tourmaline and cassiterite from the Yunlong tin deposit, Yunnan, China: Implication for migmatitic-hydrothermal fluid evolution and ore genesis. Chemical Geology, 209, 193–213, https://doi.org/10.1016/j.chemgeo.2004.04.021.

Jiang, S.Y., Radvanec, M., Nakamura, E., Palmer, M., Kobayashi, K., Zhao, H.X., and Zhao, K.D. (2008) Chemical and boron isotopic variations of tourmaline in the Hnilec granite-related hydrothermal system, Slovakia: Constraints on magmatic and metamorphic fluid evolution. Lithos, 106, 1–11, https://doi.org/10.1016/j.lithos.2008.04.004.

Kalliomäki, H., Wagner, T., Fusswinkel, T., and Sakellaris, G. (2017) Major and trace element geochemistry of tourmalines from Archean orogenic gold deposits: Proxies for the origin of gold mineralizing fluids? Ore Geology Reviews, 91, 906–927, https://doi.org/10.1016/j.oregeorev.2017.08.014.

Krienitz, M.S., Trumbull, R.B., Hellmann, A., Kolb, J., Meyer, F.M., and Wiedenbeck, M. (2008) Hydrothermal gold mineralization at the Hira Buddini gold mine, India: Constraints on fluid evolution and fluid sources from boron isotopic compositions of tourmaline. Mineralium Deposita, 43, 421–434, https://doi.org/10.1007/s00126-007-0172-0.

Leeman, W.P., Tonarini, S., Pennisi, M., and Ferrara, G. (2005) Boron isotopic variations in fumarolic condensates and thermal waters from Vulcano Island, Italy: Implications for evolution of volcanic fluids. Geochimica et Cosmochimica Acta, 69, 143–163, https://doi.org/10.1016/j.gca.2004.04.004.

Li, S.B. and Li, J.J. (1997) Characteristic of metallogenic geochemistry of Yixingzhai gold mine field, Hengshan Mt., Shanxi Province. Progress in Precambrian Research, 20, 1–21 (in Chinese).

Li, S.R., Santosh, M., Zhang, H.F., Luo, J.Y., Zhang, J.Q., Li, C.L., Song, J.Y., and Zhang, X.B. (2014) Metallogeny in response to lithospheric thinning and craton destruction: Geochemistry and U-Pb zircon chronology of the Yixingzhai gold deposit, central North China Craton. Ore Geology Reviews, 56, 457–471, https://doi.org/10.1016/j.oregeorev.2012.10.008.

Li, W.B., Qiao, X.Y., Zhang, F.H., and Zhang, L.J. (2022) Tourmaline as a potential mineral for exploring porphyry deposits: A case study of the Bilihe gold deposit in Inner Mongolia, China. Mineralium Deposita, 57, 61–82, https://doi.org/10.1007/s00126-021-01051-6.

Liebscher, A., Meixner, A., Romer, R.L., and Heinrich, W. (2005) Liquid-vapor fractionation of boron and boron isotopes: Experimental calibration at 400 °C/23 MPa to 450 °C/42 MPa. Geochimica et Cosmochimica Acta, 69, 5693–5704, https://doi.org/10.1016/j.gca.2005.07.019.

Liu, Y.S., Hu, Z.C., Gao, S., Günther, D., Xu, J., Gao, C.G., and Chen, H.H. (2008) In situ analysis of major and trace elements of anhydrous minerals by LA-ICP-MS without applying an internal standard. Chemical Geology, 257, 34–43, https://doi.org/10.1016/j.chemgeo.2008.08.004.

Lu, Y.C., Ge, L.S., Shen, W., Wang, Z.H., Guo, X.D., Wang, L., and Zhou, C.F. (2012) Characteristics of fluid inclusions of Yixingzhai gold deposit in Shanxi Province and their geological significance. Mineralium Deposita, 31, 83–93 (in Chinese).

Luo, J.Y. (2009) Genetic mineralogy and metallogenic prognosis of Yixingzhai gold deposit in Fanshi County, Shanxi Province, 138 p. Ph.D. thesis, China University of Geosciences (Beijing) (in Chinese).

Marks, M.A.W., Marschall, H.R., Schühle, P., Guth, A., Wenzel, T., Jacob, D.E., Barth, M., and Markl, G. (2013) Trace element systematics of tourmaline in pegmatitic and hydrothermal systems from the Variscan Schwarzwald (Germany): The importance of major element composition, sector zoning, and fluid or melt composition. Chemical Geology, 344, 73–90, https://doi.org/10.1016/j.chemgeo.2013.02.025.

Marschall, H.R. and Jiang, S.Y. (2011) Tourmaline isotopes: No element left behind. Elements, 7, 313–319, https://doi.org/10.2113/gselements.7.5.313.

Medaris, L.G., Fournelle, J.H., and Henry, D.J. (2003) Tourmaline-bearing quartz veins in the Baraboo Quartzite, Wisconsin: Occurrence and significance of foitite and "oxy-foitite." Canadian Mineralogist, 41, 749–758, https://doi.org/10.2113/gscanmin.41.3.749.

Mercadier, J., Richard, A., and Cathelineau, M. (2012) Boron-and magnesium-rich marine brines at the origin of giant unconformity-related uranium deposits: Δ^{11}B evidence from Mg-tourmalines. Geology, 40, 231–234, https://doi.org/10.1130/G32509.1.

Meyer, C., Wunder, B., Meixner, A., Romer, R.L., and Heinrich, W. (2008) Boron-isotope fractionation between tourmaline and fluid: An experimental re-investigation. Contributions to Mineralogy and Petrology, 156, 259–267, https://doi.org/10.1007/s00410-008-0285-1.

Migdisov, A., Williams-Jones, A.E., Brugger, J., and Caporuscio, F.A. (2016) Hydrothermal transport, deposition, and fractionation of the REE: Experimental data and thermodynamic calculations. Chemical Geology, 439, 13–42, https://doi.org/10.1016/j.chemgeo.2016.06.005.

Orlando, A., Ruggieri, G., Chiarantini, L., Montegrossi, G., and Rimondi, V. (2017) Experimental investigation of biotite-rich schist reacting with B-bearing fluids at upper crustal conditions and correlated tourmaline formation. Minerals, 7, 155, https://doi.org/10.3390/min7090155.

Pal, D.C., Trumbull, R.B., and Wiedenbeck, M. (2010) Chemical and boron isotope compositions of tourmaline from the Jaduguda U (-Cu-Fe) deposit, Singhbhum shear zone, India: Implications for the sources and evolution of mineralizing fluids. Chemical Geology, 277, 245–260, https://doi.org/10.1016/j.chemgeo.2010.08.008.

Peng, N.H., Shao, Y.J., Liu, Z.F., and Wang, C. (2017) Metallogenic mechanism of Yixingzhai gold ore field in Fanshi county, Shanxi province: Evidences from isotopes and fluid inclusion. Zhongguo Youse Jinshu Xuebao, 27, 305–317 (in Chinese).

Perugini, D. and Poli, G. (2007) Tourmaline nodules from Capo Bianco aplite (Elba Island, Italy): An example of diffusion limited aggregation growth in a magmatic system. Contributions to Mineralogy and Petrology, 153, 493–508, https://doi.org/10.1007/s00410-006-0167-3.

Pettke, T., Audétat, A., Schaltegger, U., and Heinrich, C.A. (2005) Magmatic-to-hydrothermal crystallization in the W-Sn mineralized Mole Granite (NSW, Australia). Chemical Geology, 220, 191–213, https://doi.org/10.1016/j.chemgeo.2005.02.017.

Qiao, X.Y., Li, W.B., Zhang, L.J., White, N.C., Zhang, F.H., and Yao, Z.W. (2019) Chemical and boron isotope compositions of tourmaline in the Hadamiao porphyry gold deposit, Inner Mongolia, China. Chemical Geology, 519, 39–55, https://doi.org/10.1016/j.chemgeo.2019.04.029.

Reed, M.J., Candela, P.A., and Piccoli, P.M. (2000) The distribution of rare earth elements between monzogranitic melt and the aqueous volatile phase in experimental investigations at 800 °C and 200 MPa. Contributions to Mineralogy and Petrology, 140, 251–262, https://doi.org/10.1007/s004100000182.

Rozendaal, A. and Bruwer, L. (1995) Tourmaline nodules: Indicators of hydrothermal alteration and Sn-Zn-(W) mineralization in the Cape Granite Suite, South Africa. Journal of African Earth Sciences, 21, 141–155, https://doi.org/10.1016/0899-5362(95)00088-B.

Sciuba, M., Beaudoin, G., and Makvandi, S. (2021) Chemical composition of tourmaline in orogenic gold deposits. Mineralium Deposita, 56, 537–560, https://doi.org/10.1007/s00126-020-00981-x.

Sillitoe, R.H. (2010) Porphyry copper systems. Economic Geology and the Bulletin of the Society of Economic Geologists, 105, 3–41, https://doi.org/10.2113/gsecongeo.105.1.3.

Slack, J.F. and Trumbull, R.B. (2011) Tourmaline as a recorder of ore-forming processes. Elements, 7, 321–326, https://doi.org/10.2113/gselements.7.5.321.

Spivack, A.J., Berndt, M.E., and Seyfried, W.E. Jr. (1990) Boron isotope fractionation during supercritical phase separation. Geochimica et Cosmochimica Acta, 54, 2337–2339, https://doi.org/10.1016/0016-7037(90)90060-X.

Su, Z.K., Zhao, X.F., Li, X.C., and Zhou, M.F. (2016) Using elemental and boron isotopic compositions of tourmaline to trace fluid evolutions of IOCG systems: The worldclass Dahongshan Fe Cu deposit in SW China. Chemical Geology, 441, 265–279, https://doi.org/10.1016/j.chemgeo.2016.08.030.

Sun, S.S. and McDonough, W.F. (1989) Chemical and isotopic systematics of oceanic basalts: Implications for mantle composition and processes. Special Publication, Geological Society of London, 42, 313–345, https://doi.org/10.1144/GSL.SP.1989.042.01.19.

Thomas, R., Förster, H., and Heinrich, W. (2003) The behaviour of boron in a peraluminous granite-pegmatite system and associated hydrothermal solutions: A melt and fluid-inclusion study. Contributions to Mineralogy and Petrology, 144, 457–472, https://doi.org/10.1007/s00410-002-0410-5.

Tonarini, S., Pennisi, M., Adorni Braccesi, A., Dini, A., Ferrara, G., Gonfiantini, R., Wiedenbeck, M., and Gröning, M. (2003) Intercomparison of boron isotope and concentration measurements. Part I: Selection, preparation and homogeneity tests of the intercomparison materials. Geostandards Newsletter, 27, 21–39, https://doi.org/10.1111/j.1751-908X.2003.tb00710.x.

Trumbull, R.B., Krienitz, M.S., Gottesmann, B., and Wiedenbeck, M. (2008) Chemical and boron-isotope variations in tourmalines from an S-type granite and its source rocks: The Erongo granite and tourmalinites in the Damara Belt, Namibia. Contributions to Mineralogy and Petrology, 155, 1–18, https://doi.org/10.1007/s00410-007-0227-3.

Trumbull, R.B., Beurlen, H., Wiedenbeck, M., and Soares, D.R. (2013) The diversity of B-isotope variations in tourmaline from rare-element pegmatites in the Borborema Province of Brazil. Chemical Geology, 352, 47–62, https://doi.org/10.1016/j.chemgeo.2013.05.021.

van Hinsberg, V.J., Henry, D.J., and Dutrow, B.L. (2011) Tourmaline as a petrologic forensic mineral: A unique recorder of its geologic past. Elements, 7, 327–332, https://doi.org/10.2113/gselements.7.5.327.

Veksler, I.V. and Thomas, R. (2002) An experimental study of B-, P- and F-rich synthetic granite pegmatite at 0.1 and 0.2 GPa. Contributions to Mineralogy and Petrology, 143, 673–683, https://doi.org/10.1007/s00410-002-0368-3.

Veksler, I.V., Dorfman, A.M., Dingwell, D.B., and Zotov, N. (2002) Element partitioning between immiscible borosilicate liquids: A high-temperature centrifuge study. Geochimica et Cosmochimica Acta, 66, 2603–2614, https://doi.org/10.1016/S0016-7037(02)00860-8.

Vila, T. and Sillitoe, R.H. (1991) Gold-rich porphyry systems in the Maricunga belt, northern Chile. Economic Geology and the Bulletin of the Society of Economic Geologists, 86, 1238–1260, https://doi.org/10.2113/gsecongeo.86.6.1238.

von Goerne, G., Franz, G., and Heinrich, W. (2001) Synthesis of tourmaline solid solutions in the system Na_2O-MgO-Al_2O_3-SiO_2-B_2O_3-H_2O-HCl and the distribution of Na between tourmaline and fluid at 300 to 700 °C and 200 MPa. Contributions to Mineralogy and Petrology, 141, 160–173, https://doi.org/10.1007/s004100100243.

von Goerne, G., Franz, G., and van Hinsberg, V.J. (2011) Experimental determination of Na-Ca distribution between tourmaline and fluid in the system CaO-Na_2O-MgO-Al_2O_3-SiO_2-B_2O_3-H_2O. Canadian Mineralogist, 49, 137–152, https://doi.org/10.3749/canmin.49.1.137.

Wei, C.J. (2018) Paleoproterozoic metamorphism and tectonic evolution in Wutai-Hengshan region, Trans-North China Orogen. Earth Science, 43, 24–43 (in Chinese).

Williams-Jones, A.E. and Heinrich, C.A. (2005) Vapor transport of metals and the formation of magmatic-hydrothermal ore deposits. Economic Geology and the Bulletin of the Society of Economic Geologists, 100, 1287–1312, https://doi.org/10.2113/gsecongeo.100.7.1287.

Wood, S.A. (1990) The aqueous geochemistry of the rare-earth elements and yttrium: 2. Theoretical predictions of speciation in hydrothermal solutions to 350 °C at saturation water vapor pressure. Chemical Geology, 88, 99–125, https://doi.org/10.1016/0009-2541(90)90106-H.

Wu, D.D., Li, S., Chew, D., Liu, T.Y., and Guo, D.H. (2021) Permian-Triassic magmatic evolution of granitoids from the southeastern Central Asian Orogenic Belt: Implications for accretion leading to collision. Science China. Earth Sciences, 64, 788–806, https://doi.org/10.1007/s11430-020-9714-5.

Xavier, R.P., Wiedenbeck, M., Trumbull, R.B., Dreher, A.M., Monteiro, L.V.S., Rhede, D., de Araujo, C.E.G., and Torresi, I. (2008) Tourmaline B-isotopes fingerprint marine evaporites as the source of high-salinity ore fluids in iron oxide copper-gold deposits, Carajás Mineral Province (Brazil). Geology, 36, 743–746, https://doi.org/10.1130/G24841A.1.

Yang, S.Y., Jiang, S.Y., Zhao, K.D., Dai, B.Z., and Yang, T. (2015) Tourmaline as a recorder of magmatic-hydrothermal evolution: An in situ major and trace element analysis of tourmaline from the Qitianling batholith, South China. Contributions to Mineralogy and Petrology, 170, 42, https://doi.org/10.1007/s00410-015-1195-7.

Zhai, M.G. (2011) Cratonization and the Ancient North China Continent: A summary and review. Science China. Earth Sciences, 54, 1110–1120, https://doi.org/10.1007/s11430-011-4250-x.

Zhang, L.Z. (2018) Element geochemistry and age of the altered-porphyry gold mineralization in Yixingzhai gold deposit, Fanshi city, Shanxi Province. Geology and Mineral Resources of South China, 34, 134–141 (in Chinese).

Zhang, J.Q., Li, S.R., Santosh, M., Li, Q., Niu, S.D., Li, Z.D., Zhang, X.G., and Jia, L.B. (2015) Timing and origin of Mesozoic magmatism and metallogeny in the Wutai-Hengshan region: Implications for destruction of the North China Craton. Journal of Asian Earth Sciences, 113, 677–694, https://doi.org/10.1016/j.jseaes.2015.05.004.

Zhang, J.Q., Li, S.R., Santosh, M., Niu, S.D., Li, Q., and Lu, J. (2017) The magmatic-hydrothermal mineralization systems of the Yixingzhai and Xinzhuang gold deposits in the central North China Craton. Ore Geology Reviews, 88, 416–435, https://doi.org/10.1016/j.oregeorev.2017.05.030.

Zhang, L.Z., Chen, L., Wang, G.P., Deng, X.D., and Li, J.W. (2020) Garnet U-Pb dating constraints on the timing of breccia pipes formation and genesis of gold mineralization in Yixingzhai gold deposit, Shanxi province. Earth Science, 45, 108–117 (in Chinese).

Zhao, G.C., Sun, M., Wilde, S.A., and Sanzhong, L. (2005) Late Archean to Paleoproterozoic evolution of the North China Craton: Key issues revisited. Precambrian Research, 136, 177–202, https://doi.org/10.1016/j.precamres.2004.10.002.

Zhao, H.D., Zhao, K.D., Palmer, M.R., and Jiang, S.Y. (2019) In-situ elemental and boron isotopic variations of tourmaline from the Sanfang granite, South China: Insights into magmatic-hydrothermal evolution. Chemical Geology, 504, 190–204, https://doi.org/10.1016/j.chemgeo.2018.11.013.

Zhao, H.D., Zhao, K.D., Palmer, M.R., Jiang, S.Y., and Chen, W. (2021a) Magmatic-hydrothermal mineralization processes at the Yidong tin deposit, South China: Insights from in situ chemical and boron isotope changes of tourmaline. Economic Geology and the Bulletin of the Society of Economic Geologists, 116, 1625–1647, https://doi.org/10.5382/econgeo.4868.

Zhao, K.D., Zhang, L.H., Palmer, M.R., Jiang, S.Y., Xu, C., Zhao, H.D., and Chen, W. (2021b) Chemical and boron isotopic compositions of tourmaline at the Dachang Sn-polymetallic ore district in South China: Constraints on the origin and evolution of hydrothermal fluids. Mineralium Deposita, 56, 1589–1608, https://doi.org/10.1007/s00126-021-01045-4.

Manuscript received June 8, 2023
Manuscript accepted October 18, 2023
Accepted manuscript online October 26, 2023
Manuscript handled by Fang-Zhen Teng

Endnote:

[1]Deposit item AM-24-89094. Online Materials are free to all readers. Go online, via the table of contents or article view, and find the tab or link for supplemental materials.